MODELING REAL WORLD PHENOMENA USING MOLECULAR DYNAMICS AND CONTINUUM SIMULATIONS

BY

ARCHITH RAYABHARAM

THESIS

Submitted in partial fulfillment of the requirements
for the degree of Master of Science in Aerospace Engineering
in the Graduate College of the
University of Illinois at Urbana-Champaign, 2019

Urbana, Illinois

Adviser:

Professor Deborah Levin

ABSTRACT

In the first part of this work, MD trajectory simulations of ice-like argon and amorphous silica aggregates have been performed on the HOPG and crystalline quartz surface. The ice-like argon aggregate showed tendency to deform and fragment upon contact with the surface while the more rigid amorphous SiO_2 aggregate retained its structure and gained rotational energy upon contact with the smoother HOPG surface and got accommodated or stuck when incident on the rougher quartz surface. It was observed that the final total kinetic energy retained by the aggregates decreased as the incident velocity was increased. Fragmentation was observed only from the ice-like argon aggregates. The time of emission of the fragmented Ar atoms was shorter when the ice-like argon was incident on the quartz surface compared to that obtained when the aggregate was incident on the HOPG surface. Also, more number of Ar atoms were emitted when the aggregate was incident on the quartz surface compared to that from the HOPG surface. It was observed that the sticking probability of ice-like argon aggregate is higher than that of the amorphous SiO_2 aggregate when incident on the HOPG surface. The sticking probability of SiO_2 is significantly higher than that of the ice-like argon aggregate at 1.5 km/s on the quartz surface. Dr. Levin was the supervisor for this portion of the thesis only.

In the second part of this work, two types of experimental systems have been modeled, with an aim to replicate the results of experiments and study the dynamics of the respective systems in a more detailed manner. Firstly, continuum simulations have been performed to understand a recently developed method which can potentially reduce the time required to diagnose a bacterial infection by weeks. Secondly, molecular dynamics and ab-initio molecular dynamics simulations have been performed to validate molecular-sieving of organic molecules like cyclohexane and n-hexane through carbon nanotubes. This can potentially lead to a process which can separate liquids which are otherwise very hard to separate.

TABLE OF CONTENTS

CHAPTER 1: SIMULATIONS OF SURFACE EVOLUTION DUE TO PARTICULATE-SURFACE INTERACTION

1.1 INTRODUCTION

Hypersonic flight vehicles have been a subject of research in the non-equilibrium and material science community for a number of years. Advances made in flow simulations and materials manufacturing had made it possible to design longer lasting, more efficient hypersonic vehicles. One of primary areas of use for such a vehicle is in the intelligence, surveillance, and reconnaissance (ISR) missions, as these vehicles can travel at very high speeds, gathering information from adverse terrains. Information is obtained for such a mission from viewing apertures covered by lenses, on the outer surface of the vehicle, which provide data to the electro-optical sensors housed on the vehicle. However, the boundary layer generated during a hypersonic flight contain highly corrosive gas species as well as larger dust, ice crystals, or sand particles. At hypersonic speeds, these aggregate species, even though non-reactive, will still cause significant damage to the optical lenses. Furthermore, results from the sensors are susceptible to errors due to any secondary emission that may be generated by the aggregate interactions with the lens surface.

To prevent corrosion of the lens surface due to aggregate impacts, lenses can be generally coated with thin coats of materials like HOPG. Work by Wang, *et al.*, [1] has shown that graphene coating on silicate glass was effective in protection against water damage without high losses in optical transmission. In addition, HOPG is stable and chemically inert in ambient atmosphere up to a temperature of 400^{o} C [2], which makes it an ideal candidate to be used as a coating material in high-speed flows.

In this work, we have used MD simulations to model aggregate surface interactions using trajectory simulations. The ice aggregates were approximated by considered a lennard Jones solid composed of Ar atoms, held together in a FCC structure using only van der Waals

forces. To study impacts of harder materials, trajectory simulations were also performed for an amorphous SiO_2 aggregate. To understand the effect of surface roughness on gas-particulate impacts, simulations of aggregates were bombarded on Highly Oriented Pyrolytic Graphite (HOPG) as well as quartz surfaces. HOPG and quartz are classified as atomically smooth and rough surfaces respectively and are considered as two limiting cases for this work. MD simulations allowed us to obtain detailed information regarding the post-collisional translational and rotational energies as well as fragmentation behavior of these aggregates. Sticking probabilities and surface coverage information was also obtained from MD, which will serve as an input for the micron length scale surface degradation studies to be performed using kinetic Monte Carlo (KMC) simulations.

1.2 MD NUMERICAL PARAMETERS AND DETAILS OF TRAJECTORY SIMULATIONS

All MD simulations in this work have been performed using the LAMMPS [3] MD toolkit. To study damage and contamination on the HOPG and quartz surfaces, collisions were performed using two types of aggregates, namely, ice-like argon and amorphous silica. From our previous work, [4] we know that modeling the molecular structure of ice is challenging and may require the use of computationally intensive atomic interaction potentials. Therefore, in this work, we approximate ice aggregates using "ice-like argon" aggregates, which are formed using argon atoms that are held together exclusively by van der Waals forces in order to mimic the hydrogen bonding in a frozen ice particulate.

The ice-like aggregate is made up of 38 argon atoms arranged in an FCC (face centered cubic) structure which gives it a diameter of 15.38 Å. Since the baseline van der Waals forces between argon atoms are too weak to mimic those in an ice particulate, the Lennard-Jones well depth between atoms in the ice-like argon aggregate is increased from 0.01 to 0.086 eV. [5] The amorphous silica aggregate is formed using 56 Si and 112 O atoms with

a diameter of 15.97 Å. The Si-Si, O-O, and Si-O interactions for the amorphous silica are modeled using the Tersoff potential. [6] It should be noted that both the non-covalent and covalent bonds in MD are modeled using simple harmonic oscillator. Therefore, the bonding energy is analogous to the spring stiffness or rigidity. The Si-O covalent bond strength in amorphous silica is 1.38 eV compared to the 0.086 eV non-covalent bond energy of between "ice-like" Ar atoms, which makes the amorphous silica aggregate significantly more rigid compared to the ice-like argon aggregate. Prior to performing trajectory simulations, both, ice-like argon and amorphous silica, aggregates are first energy minimized using the lowest potential energy as the criterion and then equilibrated to an internal temperature of 50 K using the Berendsen thermostat. [7]

The HOPG surface is modeled with four layers, each layer consisting of 2048 carbon atoms, with dimensions of 69.29 x 79.93 x 12.00 Å. These dimensions provide a large enough system to represent the response of the actual HOPG material to impacts due to large aggregate collisions. The -C-C- bonds of the multi-layered HOPG surface are modeled using the AI-Rebo [8] potential in LAMMPS. Similarly, the quartz surface is formed using 2268 Si and 4536 O atoms with a final size of 68.82 x 76.63 x 16.21 Å and is modeled using the Tersoff potential. [6] Prior to performing trajectory simulations, both the surfaces were first energy minimized and then equilibrated to a temperature of 677 K, representing the hot surface of a hypersonic vehicle.

The trajectory simulations were performed by bombarding the aggregates with an incidence velocity in the range of 0.5 - 1.5 km/s. This velocity range was selected based on the velocities typically observed in the boundary layer of a hypersonic vehicle. [9] The selected velocity range is expected to provide a wide spectrum of post-collisional outcomes of the aggregates such as sticking, direct scattering and fragmentation. The van der Waals forces between Ar-C, Ar-Si, Ar-O, C-O, and C-Si are modeled using the Lennard-Jones 12-6

potential energy [10],

$$V_{LJ} = 4\epsilon\left[\left(\frac{\sigma}{r}\right)^{12} - \left(\frac{\sigma}{r}\right)^{6}\right] \tag{1.1}$$

The parameters used to model surface-particulate van der Waals interactions are presented in Tab. 1.5. For all trajectories, the aggregates were modeled with an incidence angle of 90^{o}, that is, the aggregates were simulated to collide normal to the surface. A total of 2,000 trajectories were performed for each incident velocity to generate adequate statistical data. Before performing each simulation, the surface was re-equilibrated for 0.1 ps to ensures that each of the 2,000 trajectories are statistically independent.

1.3 DERIVATION OF STICKING PROBABILITY, FOOTPRINTS, COLLISION DEPTH OF THE SURFACE, AND AGGREGATE FRAGMENTATION

1.3.1 Qualitative observations from the MD trajectory simulations

Snapshots from a typical, 1.0 km/s incidence velocity trajectory simulation of ice-like argon aggregate impact on the HOPG surface are shown in Fig. 1.1. It was observed that just prior to surface impact at 2.25 ps, the ice-like argon aggregate retains its FCC crystal structure, as shown in Fig. 1.1(a). During the collision with the surface, the aggregate structure suffers significant deformation, as shown in Fig. 1.1(b). The kinetic energy exchange between the HOPG surface and the ice-like argon aggregate is sufficiently greater than the van der Waals interaction holding the ice-like argon aggregate together which causes partial fragmentation of the ice-like argon aggregate, as shown in Fig. 1.1(c). The impact of ice-like argon aggregate on the quartz surface is similar to that observed for the HOPG surface. Similar to Figs. 1.1(b) and 1.1(c), significant deformation is observed in the ice-like argon aggregate during and after the collision, as shown in Figs. 1.2(b) and 1.2(c).

In contrast, when the amorphous silica aggregate is incident on the HOPG surface with a similar 1.0 km/s incidence velocity, it does not experience significant deformation and no frag-

mentation is observed during the entire collision process, as can be seen from Figs. 1.3(a), 1.3(b), and 1.3(c). However, it was observed that during the collision with the HOPG surface, the silica aggregate gains rotational energy from the surface, as shown in Fig. 1.3(a). The gain in rotation energy was observed for all trajectories of amorphous silica impinging on HOPG surface, regardless of incidence velocity. The amorphous silica has a non-uniform geometry and as stated previously, it is significantly more rigid compared to the ice-like argon aggregate. During collision with the surface, weak LJ forces allow movement of individual argon atoms, thereby deforming the aggregate. This dissipates some of the repulsive forces exerted by the surface. However, the non-uniformity and rigidity of the amorphous silica, causes non-symmetrical reactive forces at the time of impact, which then results in the rotational energy gain by the aggregate. The stronger bond energy of SiO_2 in amorphous silica also helps retain its structure during collision with the surface and prevents fragmentation, unlike in ice-like argon. The silica aggregate continues to rotate even after moving away from the surface, as indicated by the differences in the position of atom labeled 'A' in Figs. 1.3(b) and 1.3(c).

There are differences in the post-surface silica aggregate behavior when the silica aggregate is incident on the quartz surface. Initially, as shown in Fig. 1.4(a), the amorphous silica aggregate does not deform or undergo rotation as was observed during impacts on HOPG. Instead it undergoes a phenomenon referred to as pinning, that is, the aggregate sticks to the surface, as shown in Figs. 1.4(b) and 1.4(c). The unique arrangement of Si and O atoms in the quartz structure leads to a non-planar surface topology. Unlike HOPG, multiple surface atoms do not exert either repulsive or attractive force at any given instance. Thus, at any give time during the trajectory, the repulsive force generated between a surface-aggregate atom pair will always have a counteracting attractive force between other surface-aggregate atom pairs. This leads to stationary, pinned aggregate when the silica aggregate collides with the quartz surface.

To understand the effects of incidence velocity, the collision behavior was studied by changing the incidence velocities to 0.5 and 1.5 km/s. Please note that regardless of the surface, the behavior of the silica aggregate did not change when the incidence velocity was increased, therefore, the analysis of the effect of incidence velocity is only discussed for the ice-like argon aggregate. Snapshots from typical MD simulations of the ice-like argon aggregate at the end the simulation for 0.5, 1.0, and 1.5 km/s incidence velocities, are shown in Figs. 1.5(a), 1.5(b), and 1.5(c), respectively. Even, for the lowest incidence velocity of 0.5 km/s, it was found that the ice-like argon aggregate no longer retains its FCC structure and is significantly deformed, as shown in Fig. 1.5(a). However, unlike the higher incidence velocities, the aggregate does not suffer partial fragmentation. It performs a soft landing because the energy exchange between the cluster and surface is much more gradual for an incidence velocity of 0.5 km/s, thereby preventing the constituent cluster atoms from acquiring excess kinetic energy required to fragment the cluster. As expected, increasing the incidence velocity increases the probability as well as the degree of fragmentation. As can be compared from Figs. 1.5(b) and 1.5(c), the number of Ar atoms fragmented from the ice-like argon aggregate is significantly greater when the incidence velocity was increased from 1.0 to 1.5 km/s (2 for 1 km/s and 6 for 1.5 km/s).

For the quartz surface, the ice-like argon aggregate behavior is very similar to that of ice-like argon and the HOPG surface. The ice-like argon aggregate undergoes deformation at an incidence velocity of 0.5 km/s, as shown in Fig. 1.6(a) and no longer retains the FCC structure. At higher incidence velocities, the aggregate suffers progressively severe fragmentation with increase in the incidence velocity, as shown for 1.0 and 1.5 km/s in Figs. 1.6(b) and 1.6(c), respectively.

1.3.2 Sticking probability and footprint

The scattering behavior from the two aggregates and two surface types at three incidence velocities was quantified by plotting the Z co-ordinate of the center-of-mass (COM) of the aggregates as a function of the simulation time for a few prototypical trajectories. The trajectories shown in Fig. 1.7 represent the most likely outcomes for a sample size of 2,000 trajectories of these systems with these velocities. For the ice-like argon aggregate collisions on the HOPG surface, it was observed that the most likely trajectories at 0.5 and 1.0 km/s will lead to the aggregate sticking to the surface, as shown in Fig. 1.7(a). At 1.5 km/s, however, the repulsive force on the aggregate is strong enough to repel the aggregate away from the surface. When the ice-like argon aggregate is incident on a quartz surface, similar outcomes are observed, as shown in Fig. 1.7(b). In contrast, the covalent solid amorphous silica aggregate is repelled by the HOPG surface at all incidence velocities, as shown in Fig. 1.7(c), due to combination of rigidity of the amorphous silica aggregate and the planar HOPG layer topology. When the silica aggregate is incident on the rougher quartz surface, the structure of the aggregate and the surface creates a "Velcro"-like effect, which causes all aggregates to stick to the surface, at all incidence velocities, as shown in Fig. 1.7(d).

MD simulations allow for quantifying the sticking behavior behavior by calculating the sticking probability for a particular combination of aggregate, surface and incident velocity as the ratio of the number of trajectory simulations in which the aggregates stick to the surface to the total number of trajectory simulations performed. The sticking probabilities for the argon and silica aggregates on the HOPG and silica surfaces are shown in Table 1.2. It was observed that except for the silica-quartz case, the sticking probability is highest at the lowest velocity and becomes considerably lower as the velocity is increased. These sticking probabilities will be used to model ice-like argon and sand accretion on a surface using KMC.

The collective repulsive force exerted by the surface atoms on the aggregate is directly

proportional to the incidence velocity of the aggregate. At higher velocities, aggregate atoms approach closer to the surface atoms, experiencing higher repulsive forces. The ice-like argon aggregate has the highest sticking probability when incident on the amorphous quartz surface. The comparatively weaker repulsion exerted by the multiple non-planar atoms on the surface coupled with commensurate attractive forces between the aggregate atoms on the far-side (furthest away from the surface) and the surface atoms effectively reduces the kinetic energy and stops the aggregate atoms. This generates the highest sticking probabilities. In contrast, the silica aggregate collision on HOPG generates lowest sticking probabilities. The planar topology of the HOPG surface combined with the non-deforming nature of the amorphous silica aggregate results in multiple carbon atoms exerting strong repulsion on the aggregate atoms. The rougher topology of the quartz surface and the amorphous structure of the silica aggregate lead to "Velcro"-like conditions, as discussed previously. This will predictably always force the silica aggregate to stick to the quartz surface for all incidence velocities.

The aggregate sticking behavior can be correlated with the propensity of the aggregates to deform upon contact with the surface. To quantify aggregate deformation, positions of all the aggregate atoms interacting with the surface atoms were recorded. The aggregate and surface atoms were defined to interact with each other if the inter-atomic distance was less than 6.0 Å. Next, the difference along x and y axes of the atom positions representing the minimum and maximum or extreme x and y aggregate atom positions were calculated since the surface planes are aligned in the $x - y$ plane. The difference along the x and y axes represents the semi-major and semi-minor axis of the ellipsoidal area covered by the aggregate when colliding with the surface. The coverage areas for all 2,000 trajectories for each aggregate-surface cases were calculated and was normalized by the initial projected area of the aggregate on the surface, calculated at the start of the simulation, to obtain the relative increase in the surface coverage area. The initial projected area of the aggregates is

simply a circular area equivalent to the radii of the two aggregates, which are, 185.29 and 200.30 Å^2 for the ice-like argon and amorphous silica aggregate, respectively.

The PDFs of the relative increase in the surface coverage area for the ice-like argon aggregate colliding with the HOPG surface is shown in Fig. 1.8(a). It was found that the distribution of coverage area were similar for the 0.5 and 1.0 km/s cases, while that for the 1.5 km/s was significantly different and aggregate deformation increased the coverage area by approximately 2.7 times its initial area. This is in agreement with the sticking probabilities shown in Tab. 1.2, where, the sticking probabilities are close to unity for 0.5 and 1.0 km/s but is only a tiny fraction at the highest incidence velocity. At an incidence velocity of 1.5 km/s, the ice-like argon aggregate approach closer to the surface atoms, thereby causing severe deformation of the aggregate resulting in a larger surface coverage and reducing the sticking probability of the aggregate. In comparison, the amorphous silica is more rigid and does not deform upon colliding with the HOPG surface, as evident from the comparatively lower relative increase in the surface coverage shown in Fig. 1.8(b). In line with the decreasing sticking probabilities observed with increasing incidence velocity for amorphous silica aggregates incident on the HOPG surface, the most probable surface coverage also increases with increasing incidence velocity.

The rougher quartz surface is naturally more sticky and as expected, the sticking probability of the ice-like argon aggregate on quartz is higher than that obtained for ice-like argon on HOPG at all incidence velocities, as shown in Table 1.2. At lower incidence velocities of 0.5 and 1.0 km/s, the rougher surface limits the expansion of the ice-like argon aggregates. Therefore, the relative surface coverage area at 0.5 and 1.0 km/s for the ice-like argon impacts on quartz are similar to those of ice-like argon on HOPG, as shown in Figs. 1.8(c) and 1.8(a), respectively. At the higher incidence velocity of 1.5 km/s, the ice-like argon aggregate approaches closest to the quartz surface and deforms more due to the roughness of the surface, which leads to a large increase in the relative increase in the surface coverage.

When amorphous silica aggregates collide with the surface, the irregular structure of the aggregate and the roughness of surface ensures that the aggregate sticks to the surface at all incidence velocities. This process occurs without any noticeable increase in the relative surface area covered by the aggregate. At all velocities, the distribution of relative surface coverage generated were narrow and had a peak value between 1.0 and 1.1.

1.3.3 Role of translational and internal kinetic energy on sticking and footprints

Post-collisional translational kinetic energy

The post-collision behavior for the two aggregates and two surface types at three incidence velocities were also compared by generating probability distribution functions of the ratio of final translational kinetic energy, E_{tran}, to the initial kinetic energy, E_i. The final translational kinetic energy of the cluster is expressed as,

$$E_{tran} = \frac{1}{2}\left(\sum_{i=1}^{n} m_i\right)\vec{v}_{com}^{2} \tag{1.2}$$

where, m_i is the mass of i^{th} atom, n is the number of atoms in the aggregate, and $\vec{v}_{com}$ is the center of mass velocity and its components are expressed as,

$$v_{x_{com}} = \frac{\sum_{i=1}^{n} m_i v_{x,i}}{\sum_{i=1}^{n} m_i}, \quad v_{y_{com}} = \frac{\sum_{i=1}^{n} m_i v_{y,i}}{\sum_{i=1}^{n} m_i}, \quad v_{z_{com}} = \frac{\sum_{i=1}^{n} m_i v_{z,i}}{\sum_{i=1}^{n} m_i} \tag{1.3}$$

where, $v_{x_{com}}$, $v_{y_{com}}$, $v_{z_{com}}$ are the x, y and z components of the center of mass velocity, $\vec{v}_{com}$ and $v_{x,i}$, $v_{y,i}$, $v_{z,i}$ are the x, y, z components of the velocity of the i^{th} particle in the aggregate.

The probability distribution functions (PDF) of E_{tran}/E_i, for 2,000 trajectories at each of the three incidence velocities for the ice-like argon and amorphous silica aggregate collision on the HOPG surface are shown in Fig. 1.9(a) and 1.9(b). At an incidence velocity of 0.5 and 1.0 km/s, majority of the ice-like argon aggregates lost initial kinetic energy and got

accommodated to the surface, as shown in Fig. 1.9(a), which is consistent with the sticking probabilities . While a significant number of amorphous silica aggregates also stick to the surface, majority of silica aggregates are reflected from the HOPG surface at 0.5 and 1.0 km/s incidence velocity, as shown in Fig. 1.9(b). The rigid structure of the amorphous silica discourages aggregate deformation and limits the exchange of energy between the aggregate and surface atoms. However, at an incidence velocity of 1.5 km/s, majority of the argon and silica aggregates are reflected from the surface, albeit, at a lower translational kinetic energy compared to its initial kinetic energy. As discussed previously, the higher incidence velocity allows the aggregate to come closer to the surface and therefore, experience greater repulsion from the surface atoms. From both, ice-like argon and amorphous silica interactions with the HOPG surface, it can be summarized that the aggregates has a higher chance of retaining translational energy when the incidence energy is increased.

This is in contrast to the results observed for ice-like argon and amorphous silica incident on the rougher quartz surface. As can be seen from the sticking probabilities in Tab. 1.2, the rougher quartz surface is highly effective in slowing both types of aggregates. Because ice-like aggregates at all incidence energies get trapped to the surface, the aggregates retain very little of their initial kinetic energy, as shown in Fig. 1.9(c). For the amorous silica aggregates interacting with quartz, all aggregates stick to the surface, but, amorphous silica aggregates at 0.5 km/s incidence velocity retain slightly more translational energy compared to the argon aggregates. At a lower incidence velocity, the combination of rigidity and limited number of silica aggregate atoms interacting with the surface allows slightly more energy to be retained, as shown in Fig. 1.9(d). An aggregate interacting with the quartz surface will possess limited final kinetic energies after collisions, which is leads to narrower distribution for quartz compared to that from HOPG.

Post-collisional rotational energy

From the MD trajectory snapshots shown in Figs. 1.1 - 1.4, it was observed that some of the aggregates gain rotational kinetic energy after colliding with the surface. Note that all aggregates are initialized with zero rotational kinetic energy. To quantify the gain, the rotational energy of each aggregate was calculated at the end of each trajectory as,

$$E_{rot} = \frac{1}{2}\vec{H} \cdot \vec{\omega} \tag{1.4}$$

where, $\vec{H}$ is the angular momentum of the entire aggregate and $\vec{\omega}$ is the angular velocity. The angular momentum of the aggregate is calculated using,

$$\vec{H} = \sum_{i=1}^{n} m_i[(\vec{r}_{if} - \vec{r}_{com}) \times (\vec{v}_{if} - \vec{v}_{com})] \tag{1.5}$$

where, $\vec{r}_{if}$ and $\vec{v}_{if}$ are the final position vector and velocity of the ith particle in the aggregate obtained from the MD simulations. The angular velocity of the aggregate was obtained from the product of the angular momentum and the inverse of moment of inertia tensor, $[I]$, as,

$$\vec{\omega} = [I]^{-1}\vec{H} \tag{1.6}$$

where, the moment of inertia tensor is calculated using,

$$[I] = \sum_{i=1}^{n} m_i(((\vec{r}_{if} - \vec{r}_{com}) \cdot (\vec{r}_{if} - \vec{r}_{com}))[E] - ((\vec{r}_{if} - \vec{r}_{com}) \otimes (\vec{r}_{if} - \vec{r}_{com}))) \tag{1.7}$$

and, $[E]$ is the identity tensor.

The rotational kinetic energy gain by the ice-like argon aggregate incident on the HOPG surface is shown in Fig. 1.10(a). It was observed that majority of the ice-like argon aggregates gain only a negligible amount of rotational kinetic energy. As mentioned previously,

the ice-like argon has a tendency to deform upon contact with the surface. This limits the transfer of rotational energy from the surface to the aggregate. In contrast, when the rigid amorphous silica aggregate collides with the smooth HOPG surface, the lack of deformation increases the probability of rotational kinetic energy gain from the surface, as seen in Fig. 1.10(b). While this is true at the high incidence velocity of 1.5 km/s, there is a significant fraction of aggregates which reflect from the smooth surface at lower incidence velocity, with zero rotational energy gain. This fraction becomes higher as the incidence velocity is lowered, which creates a bimodal distributions for rotation energy PDF at 0.5 and 1.0 km/s incidence velocities. For the ice-like argon aggregate incident on the rough quartz surface, the aggregate suffers fragmentation, which again limits the gain of rotational energy, as shown in Fig. 1.10(c). The proportion of rotational energy gained by the aggregates in comparison to their initial translational kinetic energy for the ice-like argon - HOPG, amorphous silica - HOPG, and ice-like argon - quartz interaction is shown in Figs. 1.11(a), 1.11(b), and 1.11(c), respectively.

Effect of incidence velocity on post-collisional aggregate energy

The post-collision behavior for the two aggregates and two surface types at three incidence velocities were also compared by generating PDFs of the ratio of final total kinetic energy to the initial value and scattering angles. To better understand the energy transfer between the aggregate-surface as well as between translation-internal modes, the final total kinetic energy of the aggregate was calculated using,

$$E_f = \sum_{i=1}^{n} \frac{1}{2} m_i \, \vec{v_f}_i^{\,2} \tag{1.8}$$

where, E_f is the final total kinetic energy, n is the total number of atoms in the aggregate, and m_i and $\vec{v_f}_i$ is the mass and final velocities of the i^{th} atom of the aggregate. To enable

comparison between trajectories with different incidence velocities, the final total kinetic energy was normalized by the initial total kinetic energy of the aggregate, E_i. The PDFs of this ratio for 2,000 trajectories at each of the three incidence velocities for the ice-like argon collision on the HOPG surface are shown in Fig. 1.12(a). For some trajectories performed with an initial velocity of 0.5 km/s, the ice-like argon aggregate even gains energy from the surface rather than losing it, as evident from values with $\frac{E_f}{E_i} > 1$. It can be observed that the relative loss of kinetic energy to internal energy of the aggregate is progressively greater as the incidence velocity is increased. At higher incidence velocities, the ice-like argon aggregate suffers deformation and fragmentation, thereby, reducing its final total kinetic energy. At 0.5 km/s, the aggregate does not fragment and due to its low initial total energy, becomes accommodated to the surface by gaining a kinetic energy equivalent to the temperature of the surface. Since majority of the aggregates stick to the surface at 0.5 km/s incidence speed, the scattering angle distribution for ice-like argon aggregate collision on HOPG is shown only for 1.0 and 1.5 km/s trajectory cases in Fig. 1.12(b). It can be seen that majority of the scattered trajectories occur at near normal angles and as the incidence velocity was increased, the scattering angle distribution became narrower. This is expected since the scattered aggregates are being reflected from an atomically smooth HOPG surface, thus limiting the scattering angle to near normal values. At higher incidence velocities, the aggregate comes closer to the surface and if the aggregate is scattered, the stronger repulsion from the surface produces a more specular-like angle of reflection.

When the PDFs of amorphous silica aggregate incident on the HOPG surface are analyzed, it was observed that the energy distributions had a significantly larger standard deviation, as shown in Fig. 1.13(a) compared to those obtained for ice-like argon incident on HOPG, shown in Fig. 1.12(a). As discussed previously, the amorphous silica aggregate has the tendency to rotate after collision and furthermore, upon colliding with an atomically smooth HOPG surface the non-deforming, rigid amorphous silica aggregates retains more of its initial energy

after colliding with the surface. This causes the energy PDFs to be much wider compared to ice-like argon. The non-deforming nature of the amorphous silica aggregates also ensures that the majority of the scattering aggregates will leave the surface at normal angles, at all incidence velocities, as shown in Fig. 1.13(b).

Analysis of the ice-like argon collision on the quartz surface reveals that the energy PDFs, shown in Fig. 1.14(a), are similar to those observed for ice-like argon aggregate impact on HOPG, shown previously in Fig. 1.12(a). Even though, the quartz surface is rougher than HOPG, the final outcomes of ice-like argon aggregates,*i.e.*, deformation and accommodation at low incidence velocity and fragmentation at high velocities, are similar on both surfaces, which leads to similar PDFs. However, at 0.5 and 1.0 km/s incidence velocities, aggregate scattering was observed not observed from the quartz surface. Therefore, only the angular PDF for 1.5 km/s trajectories is shown in Fig. 1.14(b). For the amorphous silica aggregate collision with the quartz surface, it was observed that the energy PDFs, shown in Fig. 1.15(a) exhibit trends similar to those of ice-like argon collisions with quartz, shown in Fig. 1.14(a). However, the distributions are comparatively narrower than those of ice-like argon aggregate because the loss of kinetic energy of the amorphous silica aggregate to the quartz surface is due to pinning, where, it becomes accommodated to the surface energy, regardless of its incidence energy and not due to fragmentation. Since all amorphous silica aggregates incident on the quartz surface stick to the surface, no scattering angle data was obtained.

1.3.4 Effect of incidence velocities on ice-like argon aggregate fragmentation

As previously discussed, fragmentation was observed only for the ice-like argon aggregate because of the weak non-covalent van der Waals forces holding the Ar atoms together. Note that no fragmentation was observed on either of the two surfaces at an incidence velocity of 0.5 km/s. From preliminary analysis of the trajectory snapshots, it was observed that the fragmentation of ice-like argon aggregates in terms of the number of fragmented atoms and

the time required to fragment were a function of the incidence speed. It was found that the time required for the aggregate to fragment and emit particles is inversely proportional to its incidence velocity. As shown in Fig. 1.16(a), at an incidence velocity of 1.5 km/s, when the ice-like argon aggregate is incident on the HOPG surface, the most-likely time required to fragment and emit Ar atoms is 3 ps. In contrast, at a lower incidence velocity of 1.0 km/s, the most-likely time required for fragmentation and emission increases to approximately 11 ps. The probability of emission becomes higher as the simulation progresses in time for an incidence velocity of 1.0 km/s, whereas, the probability of emission decreases with increasing simulation time for the case with an incidence velocity of 1.5 km/s. Aggregate fragmentation is a complex process, particularly for ice-like argon aggregates which are only held together by van der Waals forces. When the first Ar atom of the aggregate (*i.e.,* the one closest to the surface) interacts with the surface, the reactive forces on that atom become distributed and sensed by other atoms in the aggregate causing them to change their relative positions to each other and weaken the van der Waals forces holding the aggregate together. If the incidence velocity is lower, the Ar atoms on the far side of the aggregate (*i.e.,* the ones furthest from the surface) have sufficient time to respond to the reactive forces and change their relative motion to minimize their energies. At higher incidence velocities, because more Ar atoms interact with the surface, there is less time for this adjustment, leading to faster fragmentation and emission.

Faster fragmentation also leads to a higher probability of emission. The PDF of the number of ice-like argon atoms emitted from the aggregate after collision with the HOPG surface is shown in Fig. 1.16(b). For an incidence velocity of 1.0 km/s, it was found that while the majority of aggregates only deform and scatter with no fragmentation, a significant fraction of aggregates undergo fragmentation and emit between one to four atoms. This number increases significantly to between 2 and 10 atoms when the incidence velocity was increased to 1.5 km/s. The most-likely number of emitted atoms also increased from zero to five when

the incidence velocity was increased. The high number of emitted atoms for high incidence velocities reduces the kinetic energy of the emitted atoms. The PDF of the final-to-initial kinetic energy reveals that for an incident velocity of 1.0 km/s, the ratio is highest when the emitted atoms have a final kinetic energy of half of the agglomerate's initial kinetic energy but is reduced to less than one-tenth of its initial energy when the incidence velocity is increased to 1.5 km/s, as shown in Fig. 1.16(c). The aggregate fragmentation occurs at the expense of the kinetic energy of the aggregate and so when the aggregate breaks into a large number of atoms, the kinetic energy of the aggregate will be proportionately lower.

Similar to the ice-like argon collision on HOPG, when the aggregate was incident on the quartz surface, the time of emission was shorter at a higher incidence velocity of 1.5 km/s, compared to that for 1.0 km/s, as shown in Fig. 1.17(a). In addition, when compared to the time of emission PDF trends from the HOPG surface, the probability of emission remains high even after peak time of emission, for both, 1.0 and 1.5 km/s trajectory cases, for the quartz surface. Quartz is comparatively a rougher surface compared to HOPG, which leads to non-uniform attractive and repulsive forces between the surface and aggregate atoms during the collision. This, in turn, leads to a higher number of atoms fragmenting from the surface over a longer duration of simulation time. The rougher surface also leads to higher number of atoms emitted for similar incidence velocities. As shown in Fig. 1.17(b), at an incidence velocity of 1.0 km/s, the majority of analyzed trajectories will emit at least one Ar atom compared to no atoms emitted from the HOPG surface. At a higher incidence velocity of 1.5 km/s, the most probable number of emitted atoms increases to 7 - 12, compared to 2 - 10 atoms for the HOPG surface. The "Velcro"-like nature of the rougher quartz surface is effective in reducing the kinetic energy of the aggregate, especially at higher incidence velocity, which is when the aggregate comes closer to the surface atoms. This is evident from the PDF of the reflected energy ratio of the ice-like argon aggregate collision on the quartz surface, as shown in Fig. 1.17(c).

It is interesting to note that emission of fragmented atoms from the ice-like argon aggregate occurs closer to the 40° from the surface plane for both the surfaces, as shown in Figs. 1.18(a) and 1.19(a). Increasing the incidence velocity from 1.0 to 1.5 km/s does not change the emission polar angle or the azimuth angle. In the azimuth direction, emitted atoms do not show a bias for any particular direction but were uniform for trajectories at both incidence velocities, as shown in Figs. 1.18(b) and 1.19(b).

1.4 CONCLUSIONS

In this work, results from the analysis of the aggregate collision on surfaces are presented using the trajectory simulations of ice-like argon and amorphous silica aggregates on the HOPG and crystalline quartz surface. The aggregates were modeled at an incidence velocity of 0.5, 1.0, and 1.5 km/s. It was observed that the ice-like Ar, which is held together only by van der Waals interactions had a tendency to deform and fragment upon contact with the surface. In contrast, the stiffer, covalently bonded amorphous SiO_2 aggregate gained rotational energy upon contact with the smoother HOPG surface and got accommodated or stuck when incident on the rougher quartz surface. It was observed that when either of the aggregates are incident on the smooth HOPG surface, the final total kinetic energy distribution are similar for the two aggregates at all incidence velocities. However, the amorphous SiO_2 aggregates incident at a low velocity of 0.5 m/s gain more energy from the rougher quartz surface than the ice-like argon aggregates. It should be noted that fragmentation was observed only from the ice-like argon aggregates in the incidence velocity range used for this work. At any incidence velocity, the time of emission of the fragmented Ar atoms was shorter when the ice-like argon was incident on the quartz surface compared to that obtained when the aggregate was incident on the HOPG surface. Also, more number of Ar atoms were emitted when the aggregate was incident on the quartz surface compared to that from the HOPG surface.

It was observed that the sticking probability of ice-like argon aggregate is higher than that of the amorphous SiO_2 aggregate when incident on the HOPG surface. The smooth topology of the HOPG surface allows for larger surface for deformed Ar aggregate to stick to the surface, but the more rigid amorphous silica aggregate is repelled away from the HOPG surface. While the sticking probabilities are similar for the ice-like argon and the amorphous SiO_2 on the quartz surface, at the incidence velocity of 0.5 and 1,0 km/s, the sticking probability of SiO_2 is significantly higher than that of the ice-like argon aggregate at 1.5 km/s incidence velocity. This is because the ice-like argon aggregate fragments into multiple atoms and is repelled from the surface. The depth of surface deformation caused due to impacts with aggregates was also found to increase at higher velocities and was consistently greater for the amorphous silica aggregate due to its higher mass. The sticking probabilities, surface coverage, and surface deformation depth results obtained from the MD simulations will be used as an input to model the surface degradation for a micron length-scale grid using kinetic Monte Carlo n-fold way simulations.

1.5 TABLES AND FIGURES

Atom pairs	σ (Å)	ϵ (eV)
Ar - C	2.845	0.00627
Ar- Si	3.210	0.01120
Ar - O	3.040	0.00740
C - Si	3.700	0.00900
C - O	3.024	0.00380
C - H	2.9	0.00192
C - C	3.4	0.0066
O - H	3.166	0.0066
O - O	3.166	0.00867
H - H	2.4	0.00129

Table 1.1: Lennard-Jones parameters used to model surface-particulate interactions.

Type of interaction / velocity	0.5 km/s	1 km/s	1.5 km/s
ice-like argon - HOPG	0.9938	0.8825	0.0545
SiO_2 - HOPG	0.3416	0.1112	0.00375
ice-like argon - quartz	0.9966	0.9755	0.46
SiO_2 - quartz	1.00	1.00	1.00

Table 1.2: Sticking probabilities for the two aggregates and two surfaces as a function of initial velocity

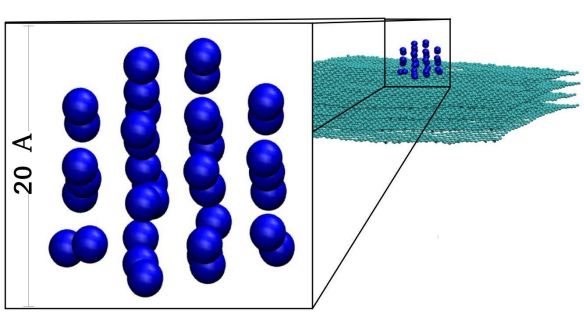

(a) At t=2.25 ps

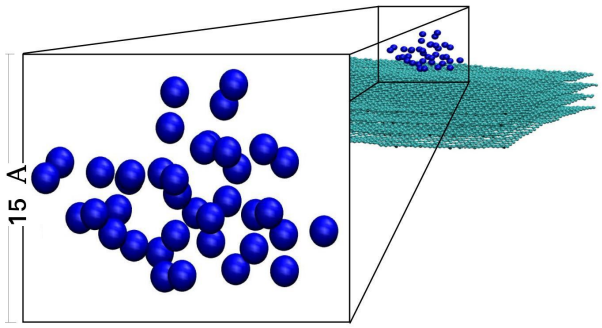

(b) At t=3.25 ps

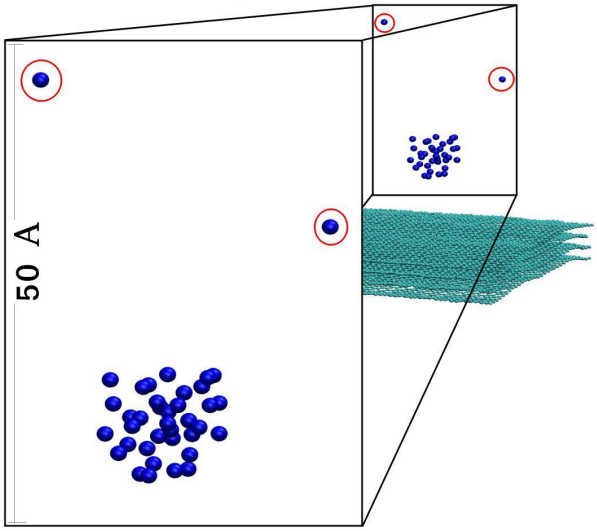

(c) At t=10.00 ps

Figure 1.1: Snapshots of cluster surface interactions between ice-like argon (blue) and HOPG (teal) at an incidence velocity of 1.0 km/s. The surface dimensions here and in subsequent figures are 69.29 x 79.93 x 12.00 Å.

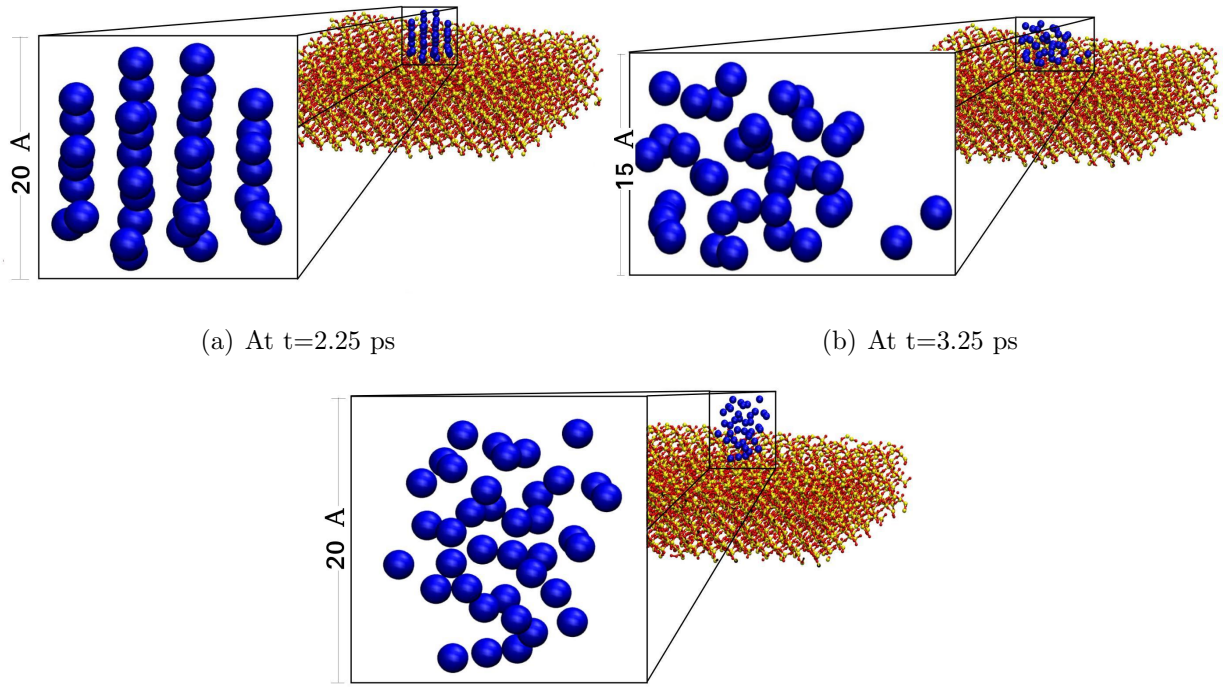

(a) At t=2.25 ps

(b) At t=3.25 ps

(c) At t=10.00 ps

Figure 1.2: Snapshots of cluster surface interactions between ice-like argon (blue) and quartz (Si in yellow and O in red) at an incidence velocity of 1.0 km/s. The surface dimensions are 68.82 x 76.63 x 16.21 Å.

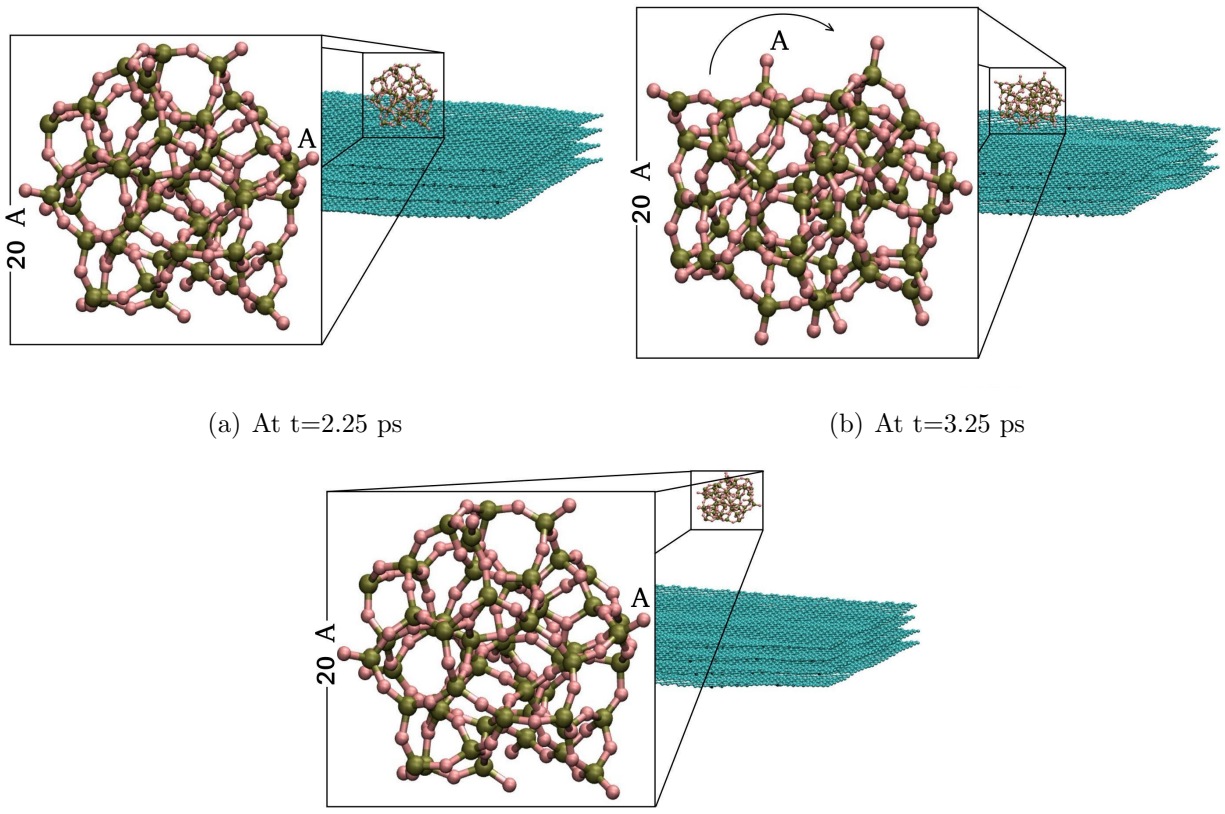

(a) At t=2.25 ps

(b) At t=3.25 ps

(c) At t=10.00 ps

Figure 1.3: Snapshots of cluster surface interactions between amorphous silica (Si in tan and O in pink) and HOPG (teal) at an incidence velocity of 1.0 km/s.

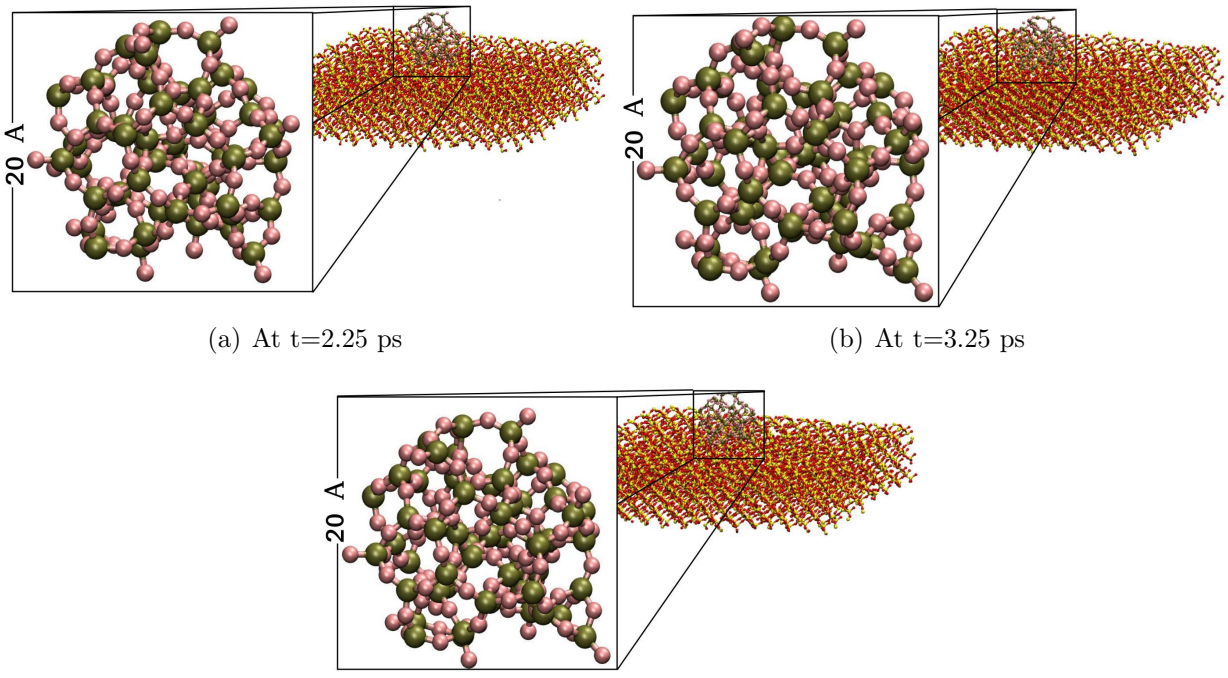

(a) At t=2.25 ps

(b) At t=3.25 ps

(c) At t=10.00 ps

Figure 1.4: Snapshots of cluster surface interactions between amorphous silica (Si in tan and O in pink) and quartz (Si in yellow and O in red) at an incidence velocity of 1.0 km/s.

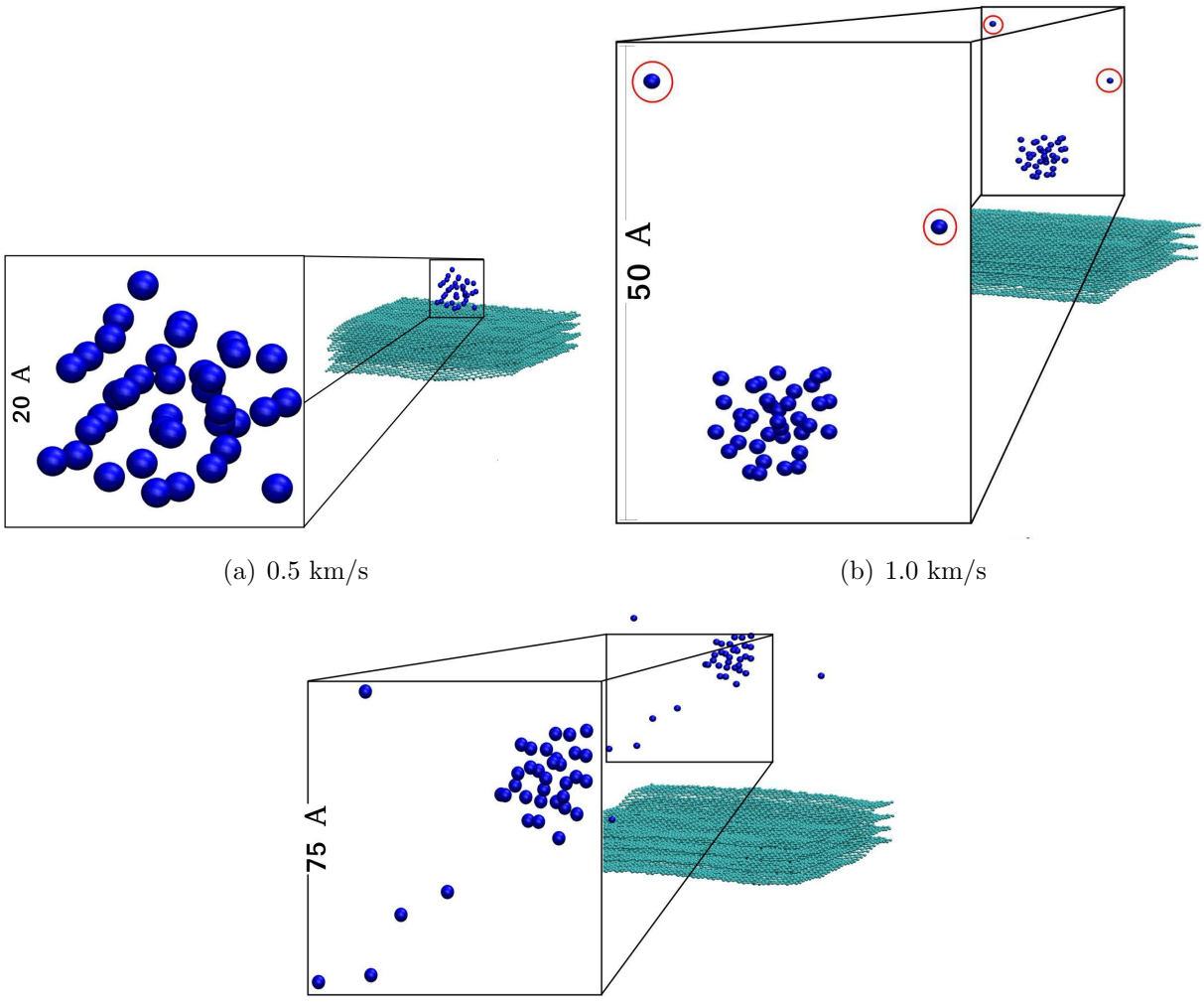

(a) 0.5 km/s

(b) 1.0 km/s

(c) 1.5 km/s

Figure 1.5: Snapshots of the final outcomes of cluster surface interactions between ice-like argon (blue) and HOPG (teal) at 10 ps as a function of incidence velocities.

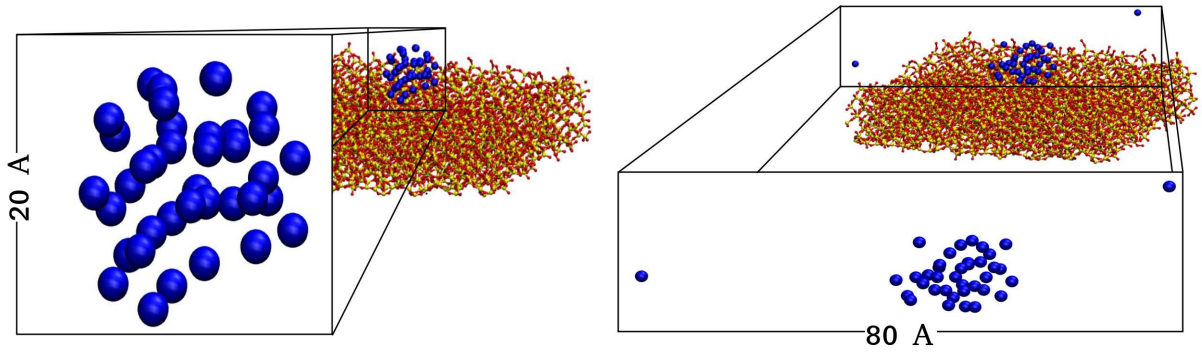

(a) 0.5 km/s

(b) 1.0 km/s

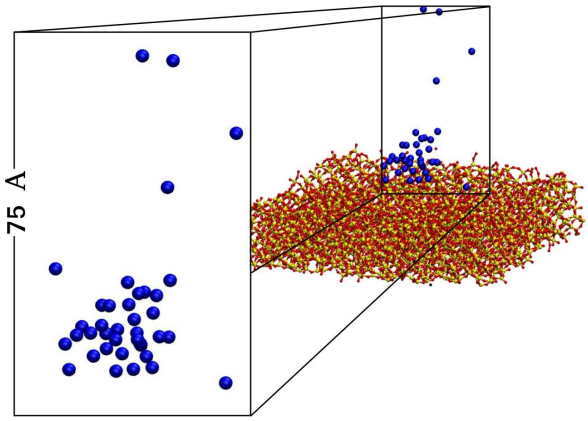

(c) 1.5 km/s

Figure 1.6: Snapshots of the final outcomes of cluster surface interactions between ice-like argon (blue) and amorphous silica at 10 ps as a function of incidence velocities.

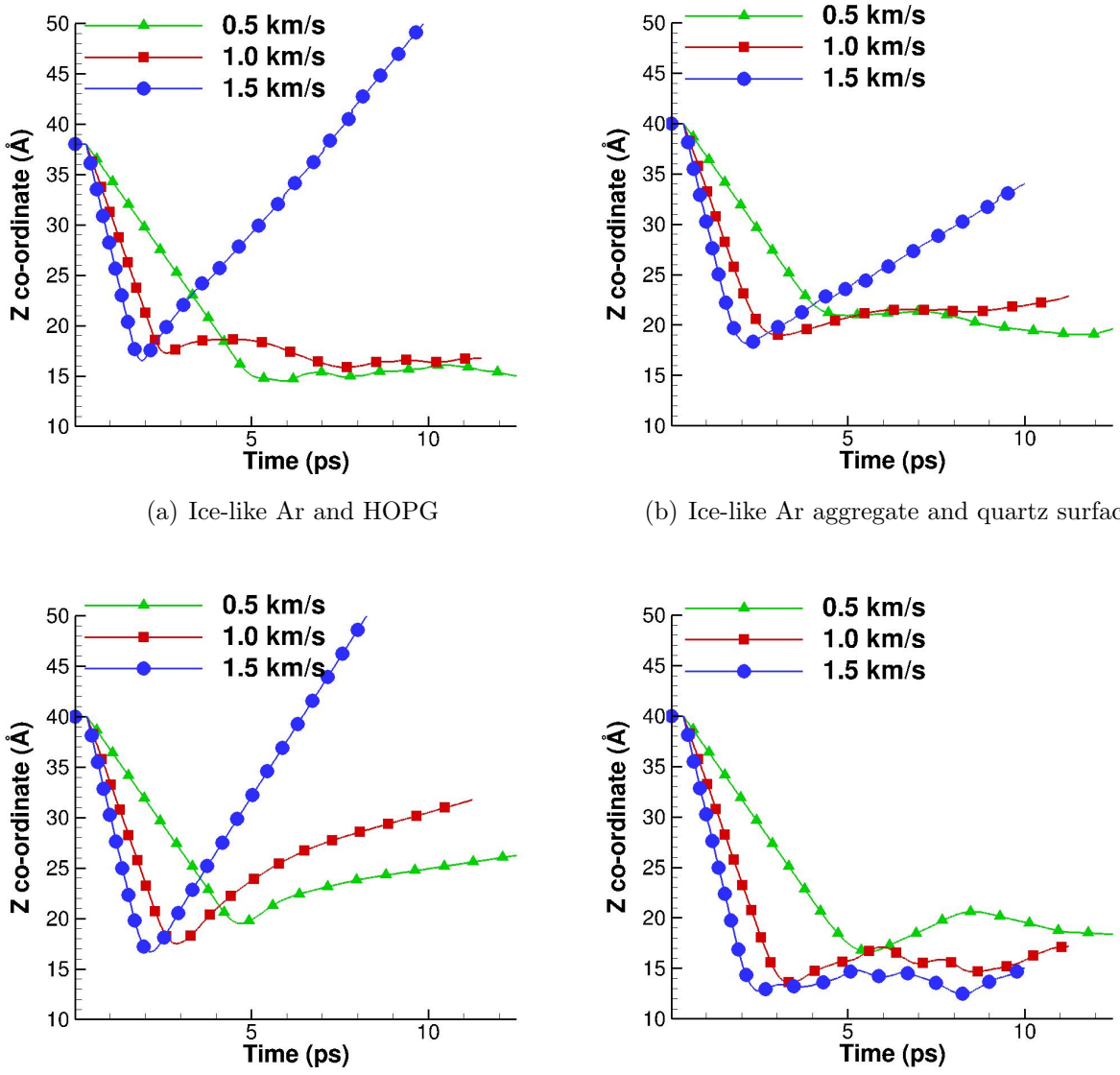

(a) Ice-like Ar and HOPG

(b) Ice-like Ar aggregate and quartz surface

(c) Amorphous silica and HOPG

(d) Amorphous silica and quartz surface

Figure 1.7: Z co-ordinate of the aggregate center-of-mass representing the most probable trajectory for two types of agglomerates and surfaces and three incident velocities.

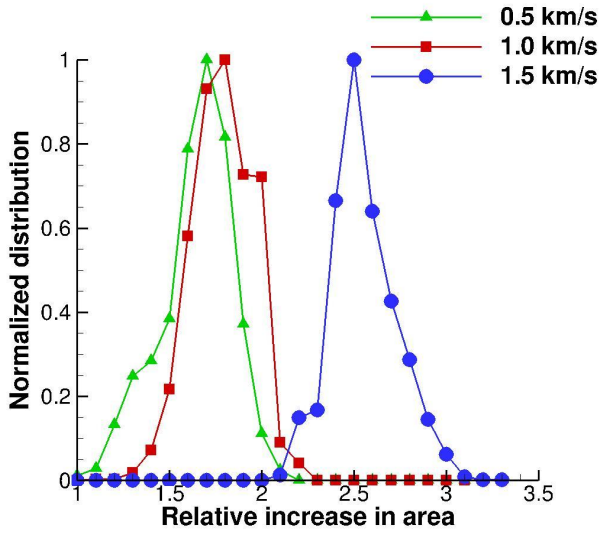

(a) Ice-like Ar aggregate incident on HOPG surface

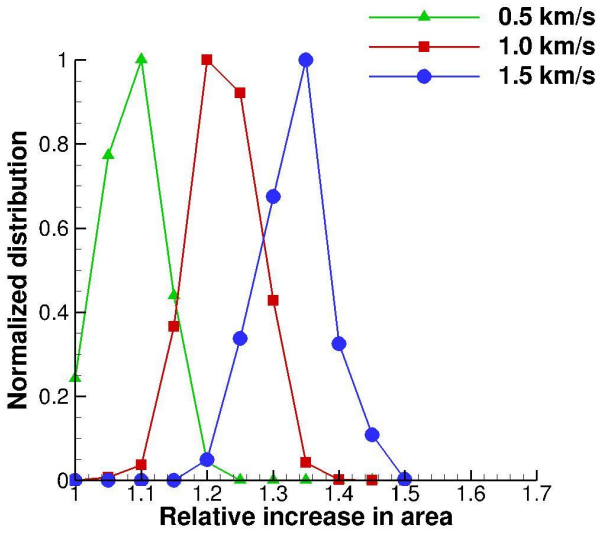

(b) Amorphous silica aggregate incident on HOPG surface

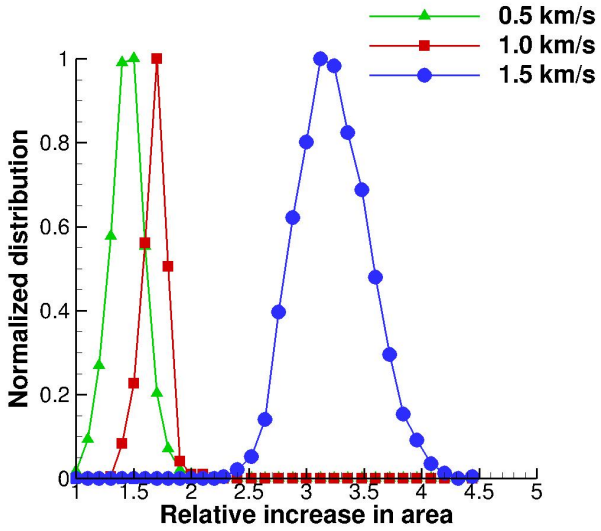

(c) Ice-like Ar aggregate incident on quartz surface

Figure 1.8: Normalized PDFs of the relative area increase in the surface coverage. The coverage area are normalized using the projected area of the aggregates, which are, 185.29 and 200.30 Å^2 for the ice-like argon and amorphous silica aggregate, respectively.

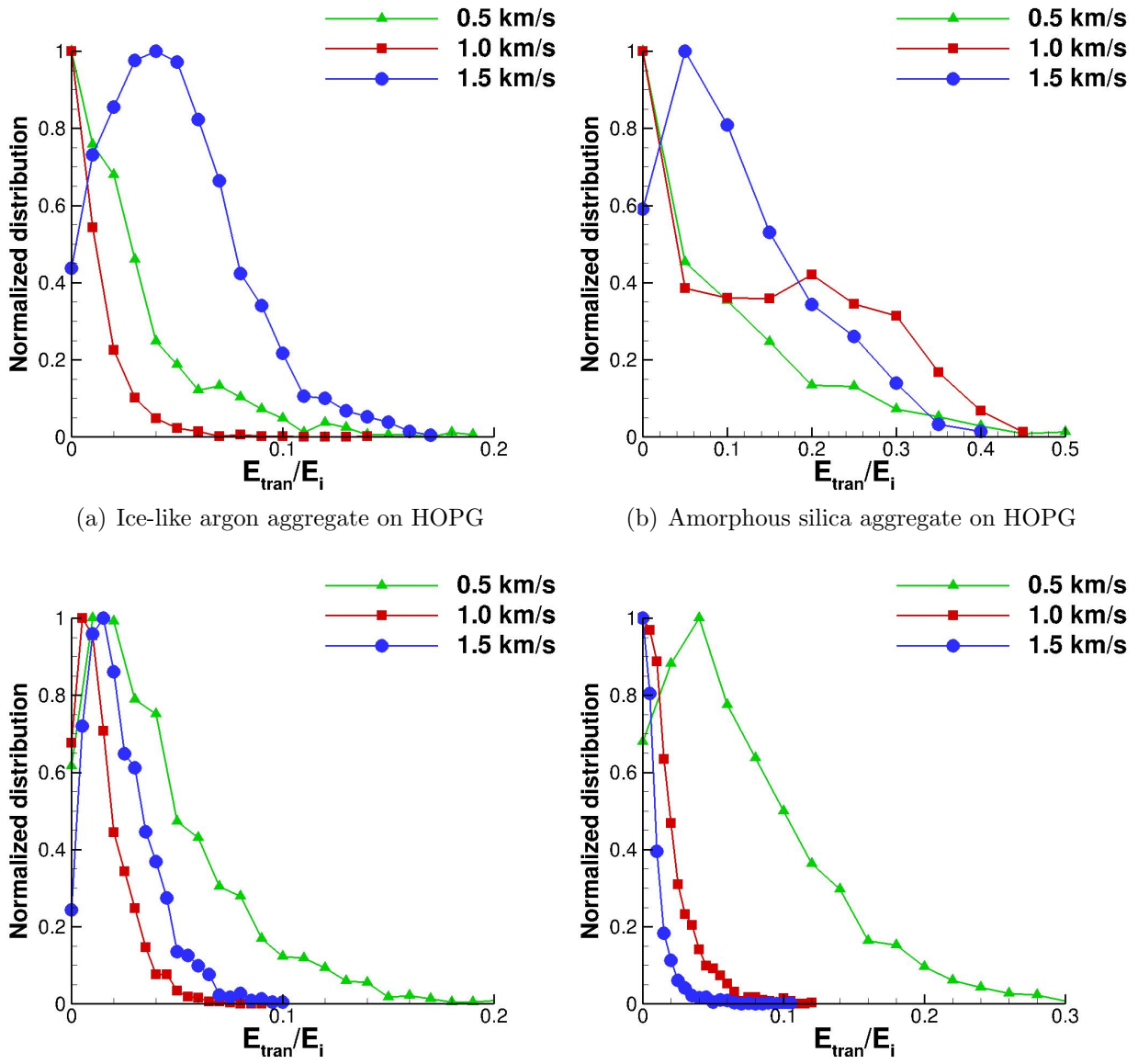

(a) Ice-like argon aggregate on HOPG

(b) Amorphous silica aggregate on HOPG

(c) Ice-like argon aggregate on quartz

(d) Amorphous silica aggregate on quartz

Figure 1.9: Normalized probability distribution functions (PDF) of ratio of reflected translational-to-total initial energies for the aggregates incident on different surfaces.

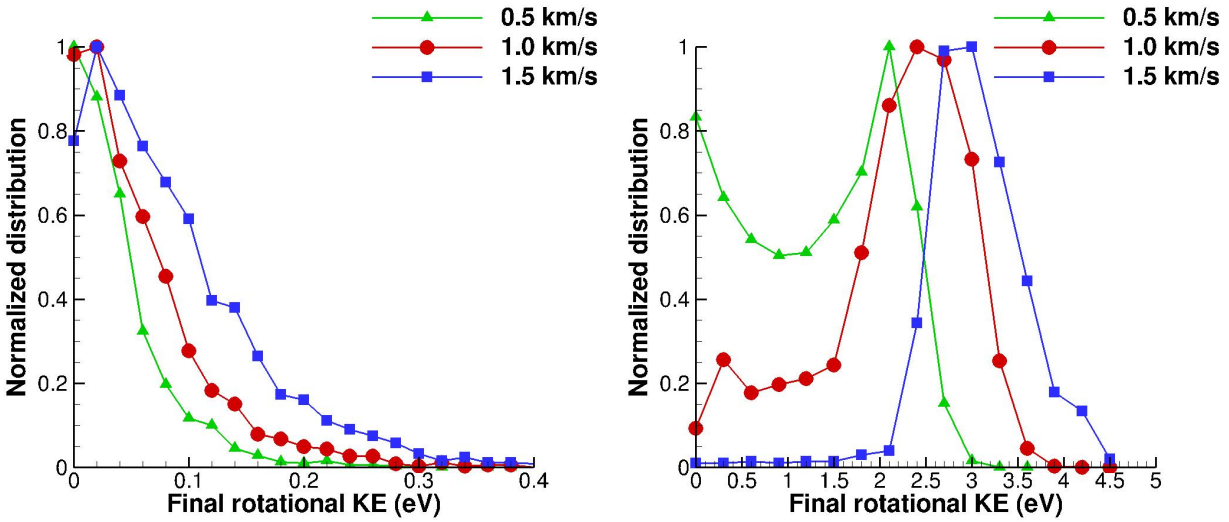

(a) Ice-like Ar aggregate incident on HOPG surface (b) Amorphous silica aggregate incident on HOPG surface

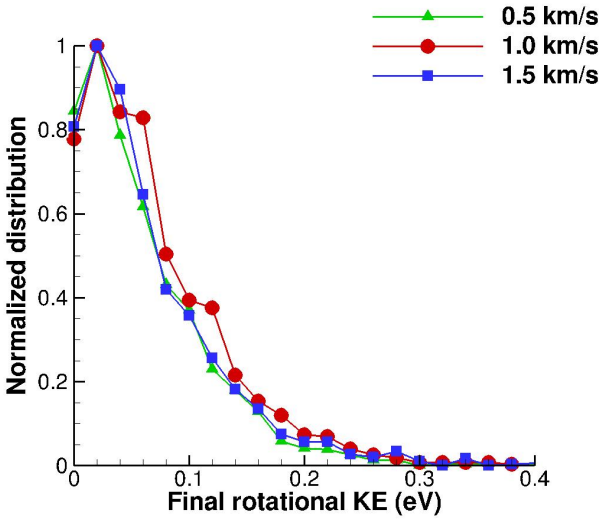

(c) Ice-like Ar aggregate incident on quartz surface

Figure 1.10: Normalized PDFs of the post-collisional rotational kinetic energy of the aggregates. The rotational kinetic energy is calculated using Eq. 1.4

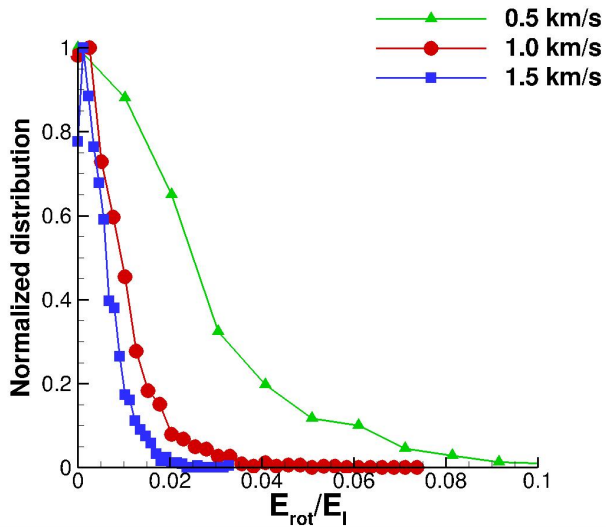

(a) Ice-like Ar aggregate incident on HOPG surface

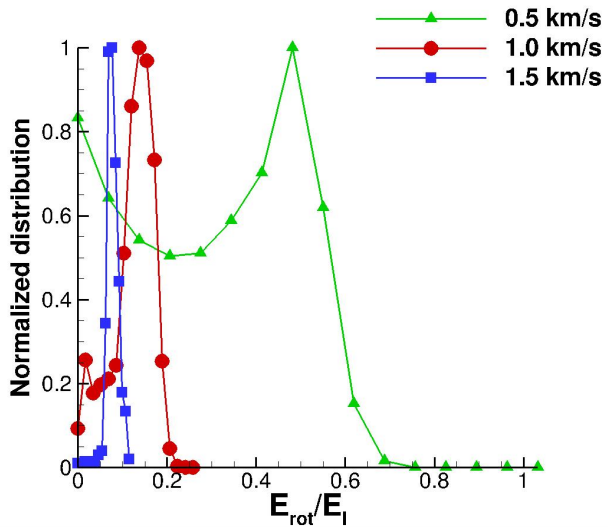

(b) Amorphous silica aggregate incident on HOPG surface

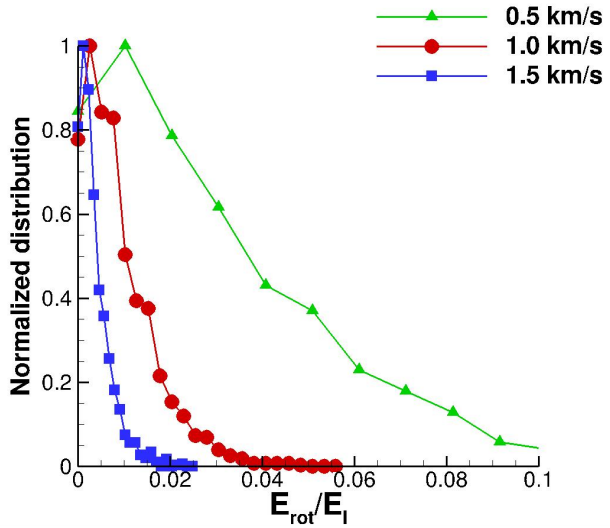

(c) Ice-like Ar aggregate incident on quartz surface

Figure 1.11: Normalized PDFs of ratio of rotational-to-initial translational kinetic energy.

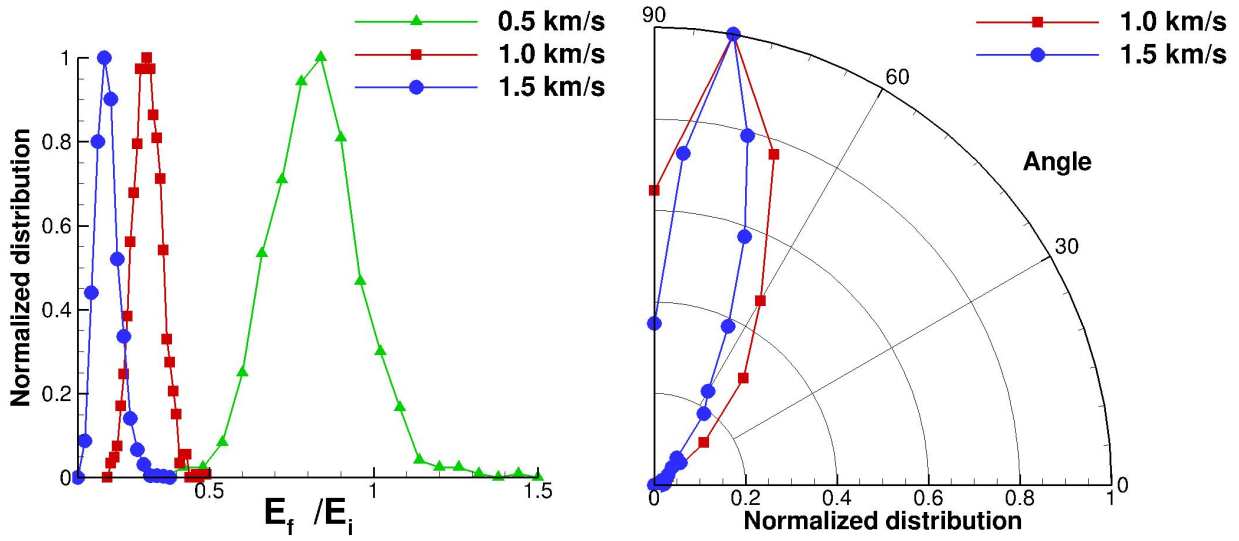

(a) PDF of ratio of reflected-to-initial kinetic energy

(b) PDF of aggregate scattering angles

Figure 1.12: Normalized probability distribution functions (PDF) for trajectory simulations of ice-like argon incident on HOPG surface. E_f is given by Eq. 1.8.

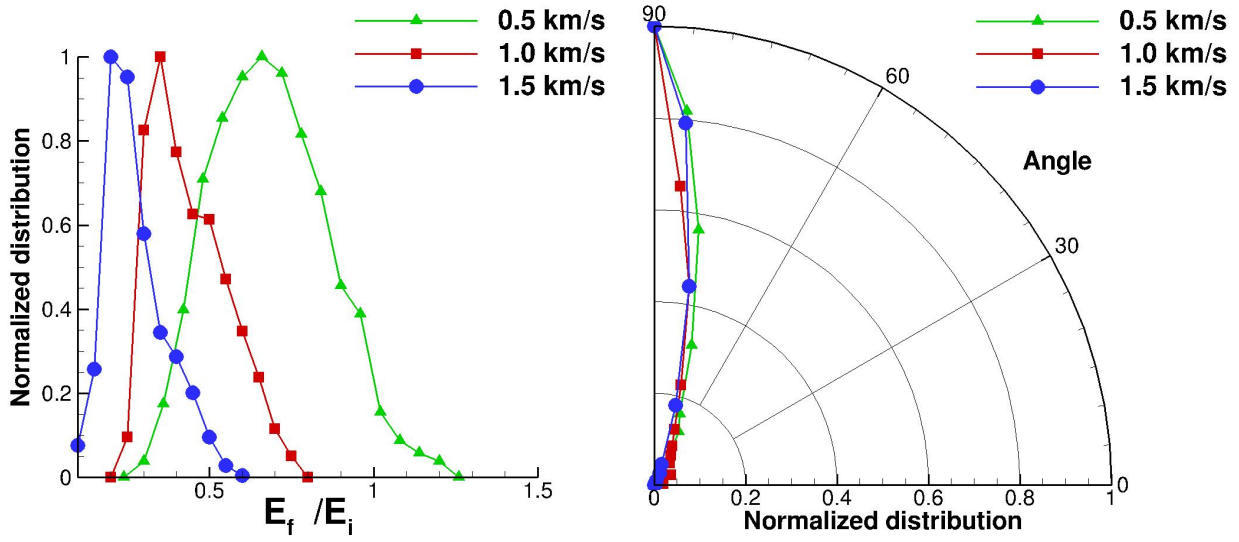

(a) PDF of ratio of reflected-to-initial kinetic energy

(b) PDF of aggregate scattering angles

Figure 1.13: Normalized probability distribution functions (PDF) for trajectory simulations of amorphous silica incident on HOPG surface. E_f is given by Eq. 1.8.

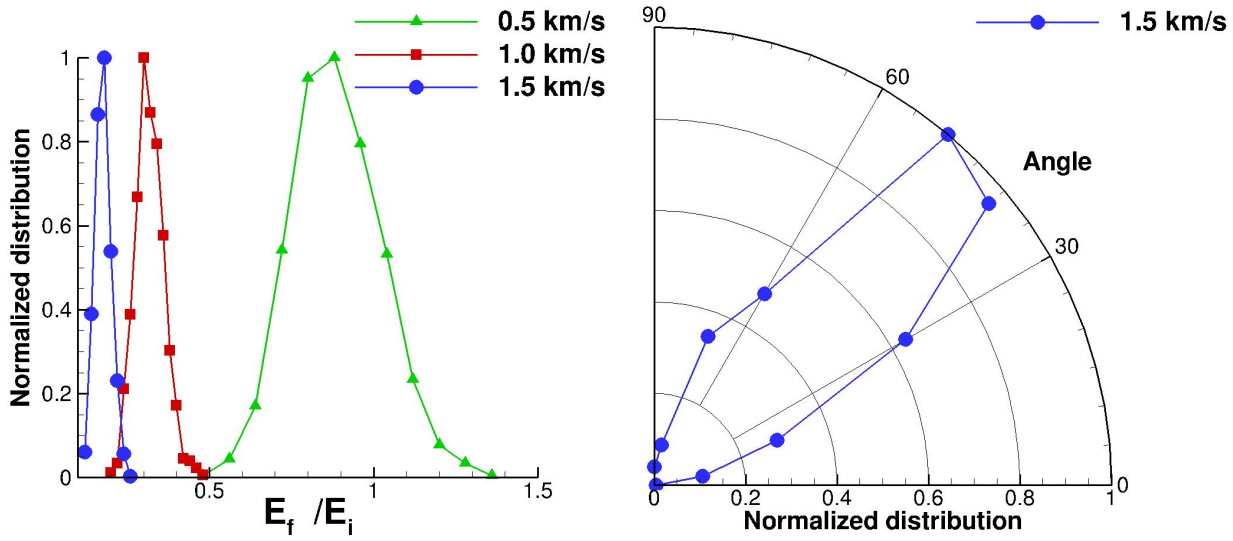

(a) PDF of ratio of reflected-to-initial kinetic energy

(b) PDF of aggregate scattering angles

Figure 1.14: Normalized probablity distribution functions (PDF) for trajectory simulations of ice-like argon incident on quartz surface. E_f is given by Eq. 1.8.

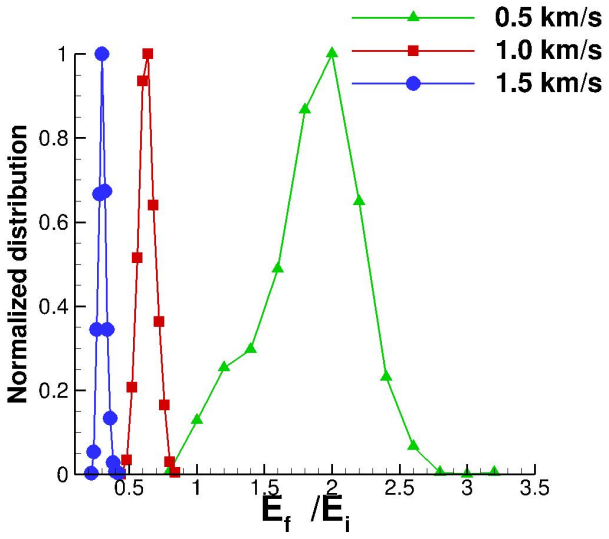

(a) PDF of ratio of reflected-to-initial kinetic energy

Figure 1.15: Normalized probability distribution functions (PDF) for trajectory simulations of amorphous silica incident on quartz surface. E_f is given by Eq. 1.8.

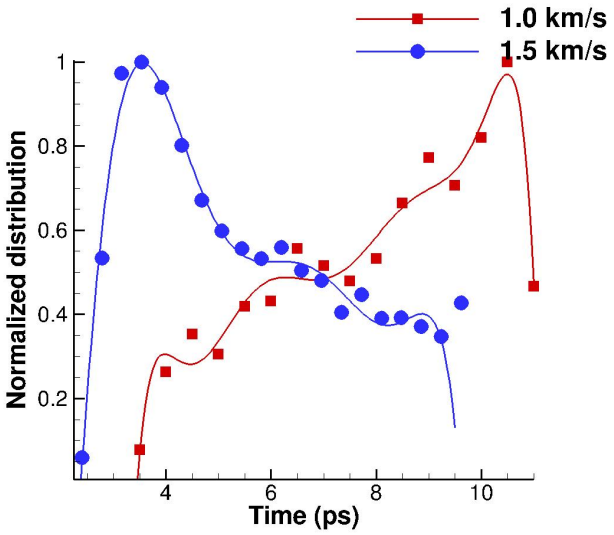

(a) PDF of the emission time

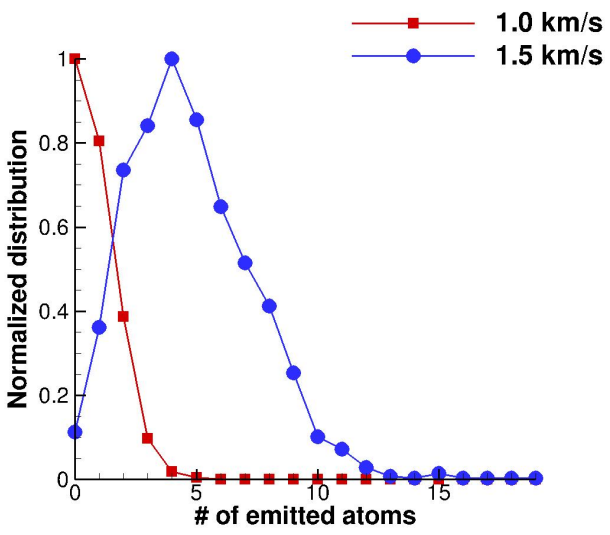

(b) PDF of the number of emitted Ar atoms

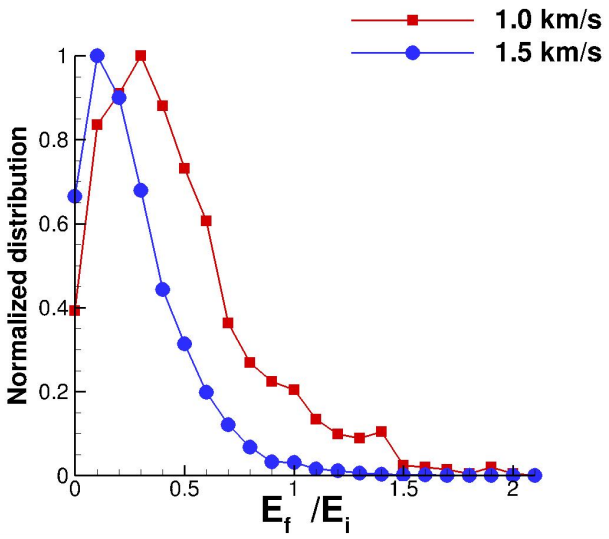

(c) PDF of ratio of average reflected-to-initial kinetic energy of emitted Ar atoms

Figure 1.16: Normalized PDFs for Ar atoms emitted from the ice-like argon aggregate after collision with the HOPG surface. Here and in the next figure, $E_i = \sum_{i=1}^{n} \frac{1}{2} m_i \vec{v}_{ii}^{\,2}$ and $E_f = \sum_{i=1}^{p} \frac{1}{2} m_i \vec{v}_{if}^{\,2}$, where p is the number of atoms emitted from the agglomerate.

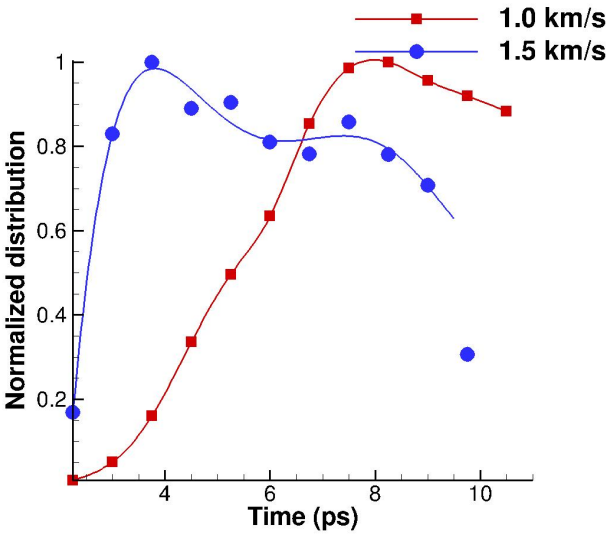

(a) PDF of the emission time

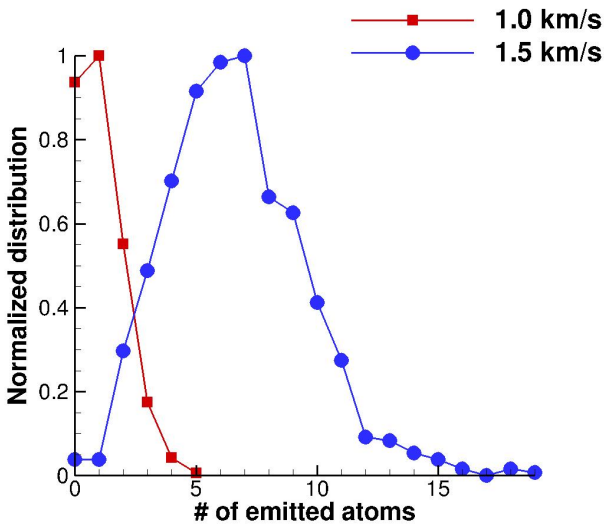

(b) PDF of the number of emitted Ar atoms

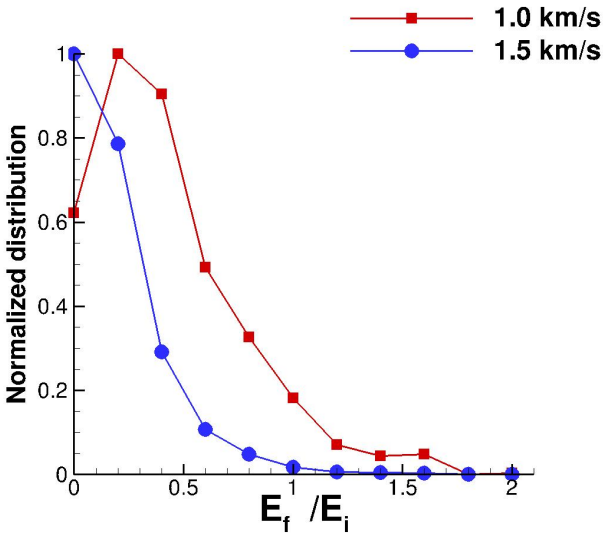

(c) PDF of ratio of average reflected-to-initial kinetic energy of emitted Ar atoms

Figure 1.17: Normalized PDFs for Ar atoms emitted from the ice-like argon aggregate after collision with the quartz surface.

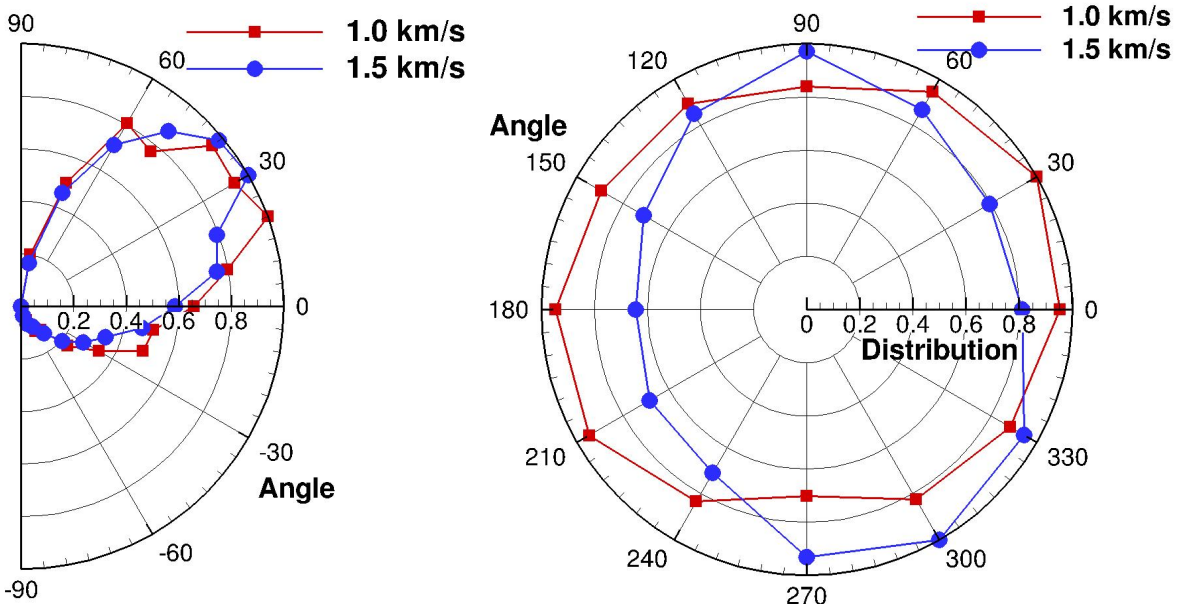

(a) Polar angle (b) Azimuth angle

Figure 1.18: Normalized PDFs of the scattering angles for Ar atoms emitted from the ice-like argon aggregate after collision with the HOPG surface.

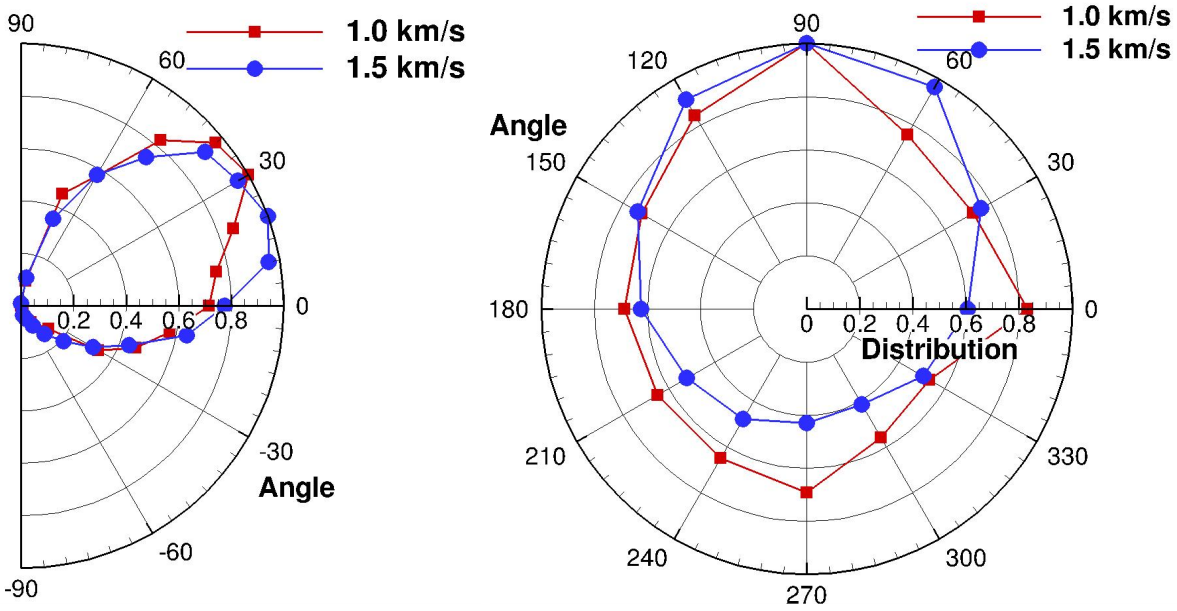

(a) Polar angle (b) Azimuth angle

Figure 1.19: Normalized PDFs of the scattering angles for Ar atoms emitted from the ice-like argon aggregate after collision with the HOPG surface.

CHAPTER 2: SIMULATIONS OF EXPERIMENTAL SYSTEMS USING MOLECULAR DYNAMICS AND CONTINUUM SIMULATIONS

2.1 CONTINUUM MODELING OF FLOW THROUGH MICROCHANNELS

2.1.1 Problem description and introduction

Currently, methods to diagnose bacterial infections involve growing cultures of bacteria. This process takes anywhere from days to weeks. In case the patient is suffering from rapid onset diseases like sepsis, he/she does not have so much time to live. Our collaborators, from the Bio-engineering department at UIUC, have developed a method to potentially reduce the time required to diagnose the pathogen from days to hours. Their method consists of adding enzymes to dried blood and artificially creating microchannels in them, by a process called elution. Then, they add a polymerase enzyme which diffuses into the microchannels, reaches the pathogen DNA and starts replicating a particular segment of the pathogen DNA. When the concentration of the pathogen DNA reaches a threshold, its DNA sequence can be identified via fluorescence measurements. The pathogen DNA does not diffuse out of the microchannels as its diffusion coefficient is 3 orders of magnitude lower than the other constituents of the sample. The reaction proceeds until all the raw materials (dNTP) have been consumed. Finally, they detect the fluorescence from the sample to identify the type of bacteria in the infected blood. The aim of this project is to verify the mechanism with which the replication reaction proceeds in the microscale porous medium.

To model this system in continuum, we can divide the experimental process into three main steps

- Elution: Perfomed at 95°C; this process is used to create the microchannels in the dried blood solution
- Diffusion: Performed at 65°C; this process consists of adding the enzymes (BST poly-

merase) and the raw materials (dNTP) to the porous dried blood matrix and allowing them to diffuse into the microchannels

- Amplification: This process consists of the reaction which takes place between the pathogen DNA and dNTP in the presence of BST polymerase, replicating a particular segment in the DNA sequence of the pathogen.

2.1.2 Simulation details

The dimensions of the experimental setup are of the order of millimeters, therefore, we use continuum simulations to model the system. We first create the geometry, which is modeled after the test tube in which the experiment is carried out. The geometry used in the simulation is shown in Fig. 2.1. To model the porous blood matrix, we perform image segmentation on SEM images provided by the experimental group and calculate porosity of the sample. The porosity of the blood matrix calculated is found to be 78%, which is modeled into the geometry. Fig.2.2 shows the SEM image of the porous blood matrix and the same image after segmentation. Further, since the experimental setup is cylindrically symmetric, it is enough to model only one slice of the test tube.

The flow and the dynamics of the system are simulated using the continuum transport equation given below. These simulations have been performed in OpenFoam with a mesh size of 0.001 mm

$$\frac{dc_i}{dt} - \nabla.(U.c_i) - \nabla.(D_i.\nabla c_i) = R_i \tag{2.1}$$

where c_i is the concentration of species i, D_i is the diffusion coefficient if species i and rate of the reaction, R_i is given by

$$R_i = \frac{ln2}{\tau} \times c_i \times 2^{\tau} \tag{2.2}$$

where τ is the time constant of the reaction. The system is maintained at 1 atm pressure.

The temperature of the system is at 95°C for the first 2 minutes of the simulation, where only the pathogen DNA is allowed to diffuse to model the elution process of the experiment. After 2 minutes, the temperature is maintained at 65°C. The system is modelled using 2 species, namely the BST polymerase enzyme and the pathogen DNA. These species are assumed to be in aqueous medium, though the actual experimental setup consists of a buffer solution. The buffer solution does not effect the rate of the replication reaction and therefore is not modeled.

Rates of reaction for BST polymerase in aqueous medium have been documented very well [11], but in a porous medium, these rates of reactions are bound to change. To be able to predict the time required for amplification in a porous blood matrix, we use the experimental data to come up with an empirical rate equation, which can be used to predict how the reaction proceeds in similar media. This empirical rate equation is compared with the theoretical rate mentioned in Eq. 2.2 and will be used to predict the times of amplification for similar reactions in different geometries.

2.1.3 Results and discussion

In our simulations, the location of the pathogen DNA is varied and the simulation is carried out for different distances. In all the simulations, we see that only the enzyme (BST polymerase) and the raw materials (dNTP) diffuse into the microchannels, reach the DNA and start the replication reaction, whereas the pathogen DNA does not diffuse. This is because the pathogen DNA has a diffusion coefficient which is three orders of magnitude smaller than that of the other components of the system (pathogen DNA has close to 2 million bases compared to 150 bases for dNTP and BST polymerase). As we can see from Eq. 2.2, the rate equation is an exponential reaction and therefore, after reaching a threshold, the concentration of the pathogen DNA increases dramatically. This can be seen in Fig. **??** The stabilization of concentration of the pathogen DNA upon consumption of the raw materials

is not captured in the simulation as we do not incorporate this effect into our rate equation. To capture this, we model an empirical rate equation from the experimental data.

The empirical rate equation is calculated from the experimental data by normalizing the data and fitting it to a sigmoidal curve of the form :

$$R_i = 0.00242 \times \exp(\frac{1}{1+k}) \times \frac{k}{(1+k)^2};\ k = 2^{\frac{-(t-1749)}{166.32}} \tag{2.3}$$

Fig. 2.4 shows the comparison between the average experimental rate equation, which has been calculated from the raw experimental data and the empirical rate equation, modeled using Eq. 2.3. Fig. 2.3 shows the comparison between experimental and empirical concentration vs time curves. We see that the trend of the curves is captured very well, though some discrepancies are observed in the time required for amplification. The empirical rate equation overpredicts the time required for amplification by around 20 minutes.

As mentioned above, the location of pathogen DNA inside the blood matrix is varied and simulations are performed for various distances for the two rate equations. Fig. 2.5 shows the comparison between time required for amplification for the two rate equations used. The plot is parabolic as expected from the transport equation used in the simulations (Eq. 2.1). We see that the theoretical rate equation in Eq. 2.2 predicts the time required for amplification from experiments in Fig. 2.3 very well, and as mentioned above, the empirical model overpredicts this by 20 minutes.

2.1.4 Future Work

From Fig. 2.5, we see that our empirical rate equation overpredicts the time required for amplification by 20 minutes. This rate equation therefore needs to be improved and incorporated into the continuum solutions. This empirical rate equation will further be used to predict the times required for amplification in various other geometries in the same

medium.

2.2 MOLECULAR SIEVING USING CARBON NANOTUBES (CNTS)

2.2.1 Problem Description and Introduction

This project is in collaboration with the Chemistry department at University of Maryland. Experimentally, it is observed that cyclohexane (size: 0.54 nm) spontaneously enters into CNT(6,5), which has a diameter of 0.747 nm. They observe that upon doing photoluminescence spectroscopy, emission peaks shift upon incubating CNT(6,5) in a cyclohexane bath (with 99.9 % purity). They attribute this shift with the presence of cyclohexane or an impurity in the sample like n-hexane inside the tube. But, cyclohexane might be too large to enter CNT(6,5) as its pore size is estimated to be around 0.407 nm. Using molecular dynamics simulations, we want to find verify whether the molecules inside the CNT are indeed cyclohexane. In case cyclohexane does not enter the CNT (6,5), but n-hexane does, we can use this method to sieve organic compounds which otherwise are extremely difficult to separate.

Carbon nanotubes are allotropes of carbon, which can be thought of as graphene sheets rolled into cylinders. Carbon nanotubes can have a wide range of diameters and chiralities [12]. They also have different optical and electrical properties depending on their chirality and therefore have many potential applications in engineering [13], with the most attractive being desalination and ion-selective fluid transport.

2.2.2 Simulation Details: Molecular Dynamics and Ab-initio molecular dynamics

Two sets of simulations were done to model the experimental system, namely Molecular Dynamics and Ab-initio molecular dynamics (AIMD). MD simulations were performed using the LAMMPS [3] MD toolkit and AIMD using VASP [14, 15, 16, 17].

We simulate two types of organic molecules in our simulations, n-hexane and cyclohexane. These molecules are chosen due to the fact that they are commonly used organic solvents. To simulate organic molecules, we use the OPLS-AA potential [18] to model carbon-carbon and carbon-hydrogen interactions. Interactions between carbon in CNT and carbon and hydrogen in hexane and cylohexane are modeled using Lennard-Jones potential [10] with parameters mentioned in Tab. 1.5. The CNTs are terminated using -OH groups to replicate the experimental process. The system setup is shown in Fig. 2.6. The pressure is maintained at 1 atm and temperature at 300 K to accurately model the experimental conditions.

Ab-initio molecular dynamics simulations were performed for the cyclohexane, hexane and CNT(6,5) system, with CNTs terminated with hydroxyl groups (-OH) under the framework of the LDA approximation[19]. A timestep of 0.25 fs was used and the system was run for 100 ps.

2.2.3 Results and discussion

In our simulations, we observe that the minimum diameter of CNT required for cyclohexane to enter is 5.3 Åand for hexane is 4.3 Å. So in the experimental sample of CNTs, we can conclude that cyclohexane enters in CNT(10,2) and CNT(7,5), whereas n-hexane enters through CNT(8,3) and higher diameters. Tab.2.3 mentions the diameter and pore size of all the CNTs present in the sample and whether the organic molecules in consideration enter the corresponding CNTs. It has to be noted that the size of cyclohexane and hexane are 5.4 $\mathring{A}$ and 4.4 $\mathring{A}$ respectively. These molecules enter CNTs with a smaller diameter because of two reasons. Firstly, CNTs are terminated with hydroxyl groups and this increases the diameter of the CNT at the mouth of the tube. Secondly, the CNTs naturally ripple and therefore the diameter of a particular CNT oscillates about an equilibrium value. So, at the extreme ends of the oscillation, the nanotube pore is large enough for the molecules to enter.

Radial Breathing Mode (RBM) calculations

The atoms in a CNT vibrate in-phase in the radial direction. This vibration has a certain frequency to it, which is dependent on the radius of the CNT (and thereby chirality). Therfore we can assign the chirality of a CNT using its radial breathing mode. This mode of vibration can be experimentally observed using Raman spectroscopy. Further, presence of molecules inside the CNT shifts the RBM peak, which can be used to identify the type of molecule trapped inside the CNT.

We calculate the radial breathing mode from our simulations and compare them with experiments. Calculation of RBM is done using the following steps [20, 21, 22]. Velocities of carbon atoms in the CNT are first projected onto the radial direction and averaged over all carbon atoms to obtain the average radial velocity of CNT, v_r, for each timestep. Then, the auto-correlation of the average radial velocity, $C(t)$, is computed by the following equation,

$$C(t) = \frac{< v_r(t)v_r(0) >}{< v_r(0)v_r(0) >} \tag{2.4}$$

where $v_r(0)$ and $v_r(t)$ are the average radial velocity of CNT at the initial timestep(t = 0) and at time t respectively. ¡¿ denotes he average over 200 trajectory simulations with different initial velocity profiles. The spectral power density S(ω) is given by the following equation,

$$S(\omega) = \int_0^\infty C(t)cos(\omega t)dt \tag{2.5}$$

where $\omega = 2\pi f$ and f is the discrete frequency index. The RBM frequency of the CNT corresponds to the peak in the spectral power density.

Our calculations of RBM are first benchmarked with CNT(22,0) and compared with a similar simulation result as discussed in Wu, et al.[22], obtaining a peak of 133.4 compared to 133.1 in their simulations. Further, experimentally, RBM frequency as a function of the

diameter of CNT is given by the equation

$$f_{RBM} = \frac{C_1}{d} \tag{2.6}$$

where C_1 is given by 223.8 nm.cm^{-1},

Substituting the diameter of CNT(22,0) (1.7226 nm) in this equation, we get an RBM frequency of 129.91 cm^{-1}. Both these values match very well with our simulations.

Fig.2.7 shows the RBM shifts between empty CNT(6,5) and CNT(6,5) filled with cyclohexane. The RBM peak for the filled CNT(6,5) is obtained by fitting a Gaussian curve. We see that the peak shifts from 304.2 cm^{-1} to 319.4 cm^{-1} when CNT(6,5) is filled with cyclohexane. This shift matches well with the Raman spectra obtained from experiments.

Distribution of distance between CNT(6,5) and cyclohexane and hexane

To conclusively show that n-hexane and cyclohexane cannot enter into CNT(6,5), we performed AIMD simulations to calculate the distribution of distance between atoms of the organic molecules and the carbon atoms of CNT(6,5) when these molecules are forced inside the nanotube. Figs. 2.8(a) and 2.8(b) show this distribution of distance between carbon atoms of CNT(6,5) and carbon and hydrogen atoms of cyclohexane and n-hexane respectively. We see that the carbon-carbon distance for cyclohexane and n-hexane peak at 2.7 and 3.4 respectively, whereas carbon-hydrogen distances for cyclohexane and n-hexane peak at 2.1 and 2.4 respectively. It is to be noted that σ of C-C and C-H interactions are 3.4 and 2.9 respectively, as mentioned in Tab.1.5. This strongly suggests that these molecules will be experiencing very large repulsive forces inside CNT(6,5) and therefore would not go into the CNT.

2.2.4 Future work

The parameters required to model force-fields used in this work are modeled for molecules in bulk and at standard temperature and pressure of 300 K and 1 atm. But in nano-confinement regimes like flow of molecules through CNTs, quantum effects due to curvature of CNTs become significant and these parameters can no longer be used to accurately predict the flow properties. To address this, Lennard-Jones force-field parameters will be optimized using Density Functional Theory and used in MD simulations, to try and validate the experimental results.

2.3 TABLE AND FIGURES

Chirality	Diameter(Å)	Pore size(Å)	Cyclohexane enters?	n-hexane enters?
(6,4)	6.826	3.426	No	No
(6,5)	7.469	4.07	No	No
(8,3)	7.712	4.311	No	Yes
(7,5)	8.175	4.775	No	Yes
(8,4)	8.826	4.886	No	Yes
(10,2)	8.719	5.319	Yes	Yes
(7,6)	8.824	5.424	Yes	Yes

Table 2.1: Chirality and diameter of carbon nano-tubes present in the sample used by experiments

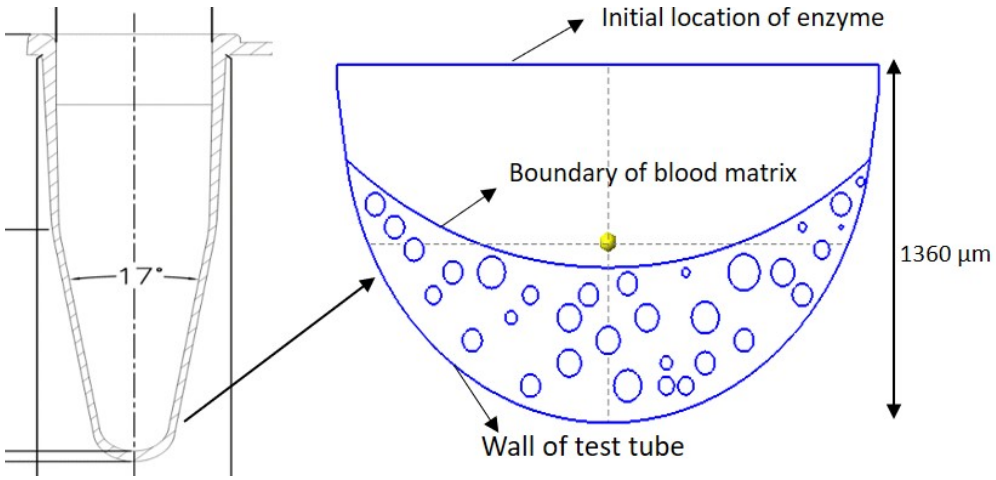

Figure 2.1: System geometry, modeled after the base of the test tube used in experiments

.

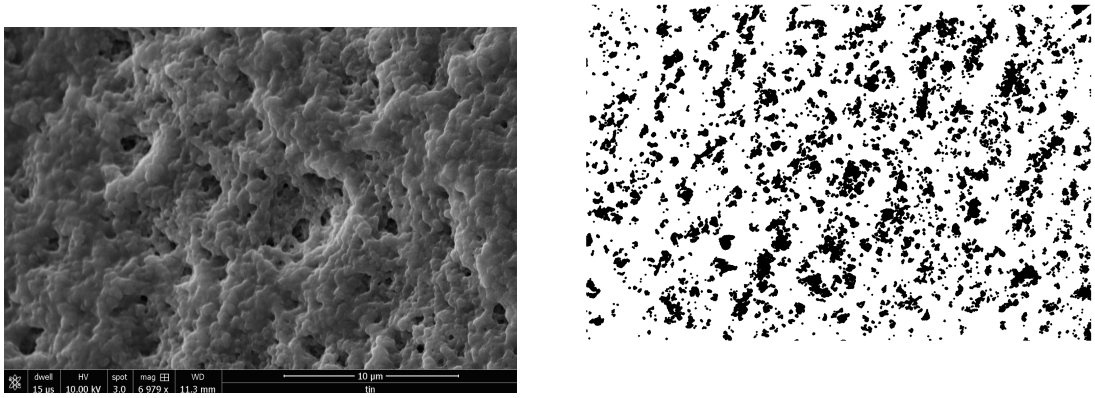

(a) SEM image (b) After image segmentation

Figure 2.2: Image segmentation performed on SEM images of the blood matrix

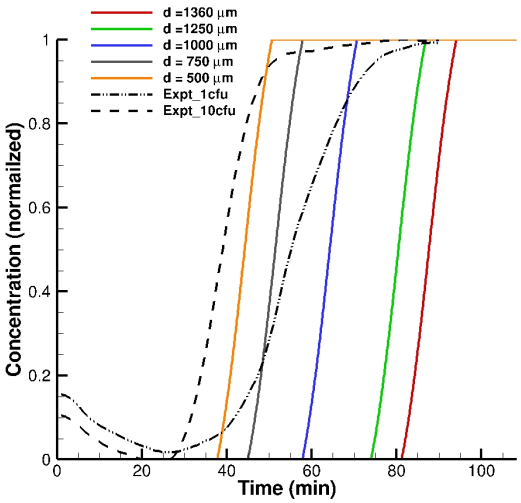

Figure 2.3: Comparison between concentration curves between averaged experimental and empirical rates

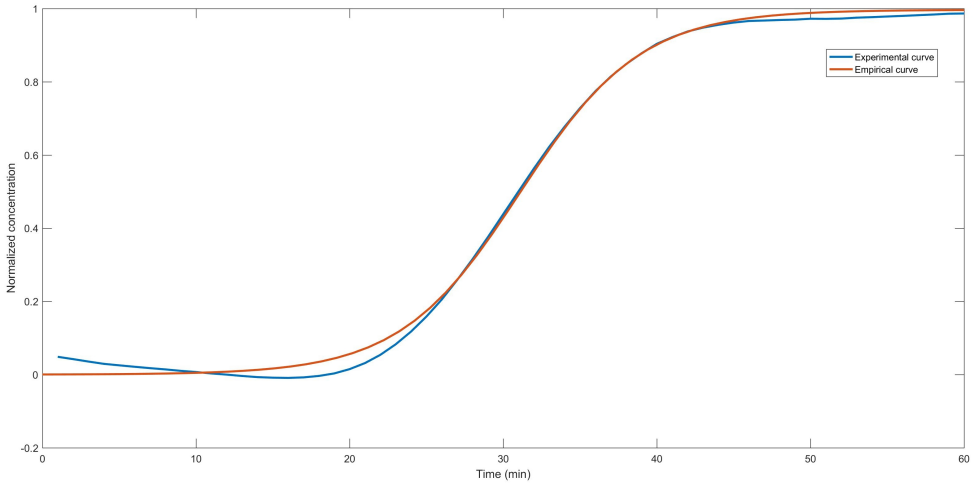

Figure 2.4: Comparison between empirical and experimental rate equations

.

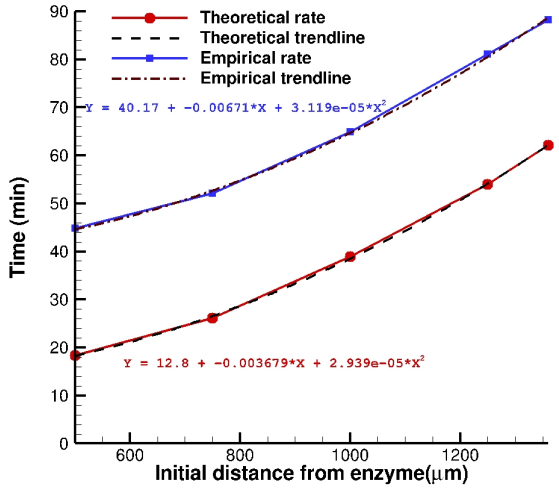

Figure 2.5: Comparison of distance vs time of amplification between theoretical and empirical rates of reaction

.

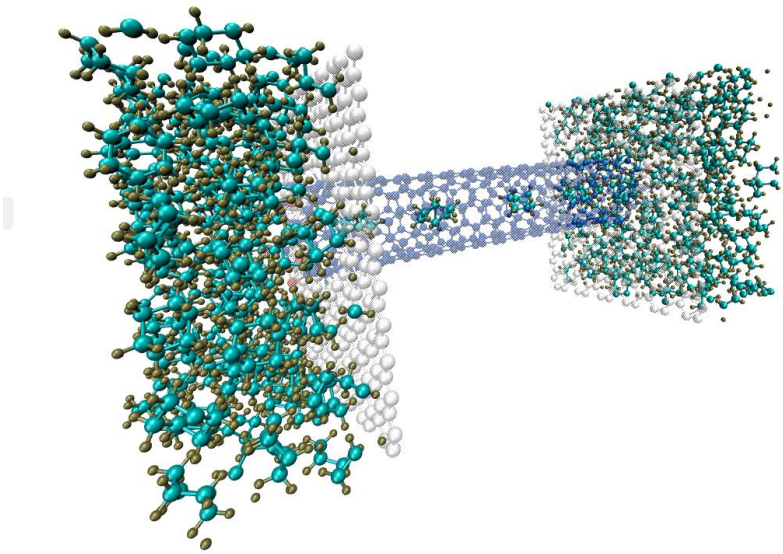

Figure 2.6: System description. Carbon and hydrogen of cyclohexane marked in teal and brown respectively, CNT in blue, graphene walls in white

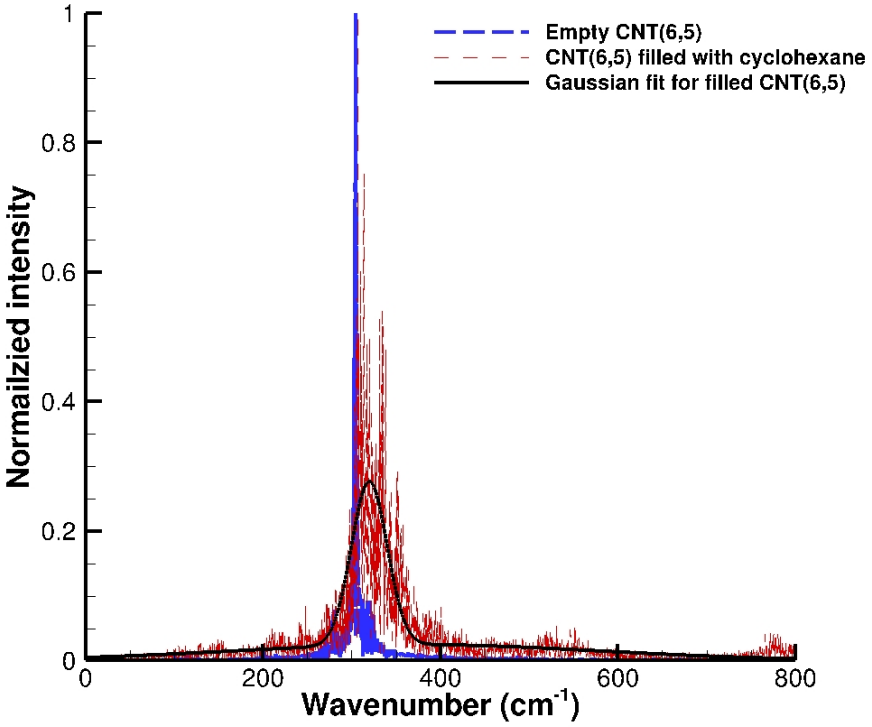

Figure 2.7: RBM shift observed in CNT(6,5) when filled with, peak shifts from 304.2 cm^{-1} to 319.4 cm^{-1}

.

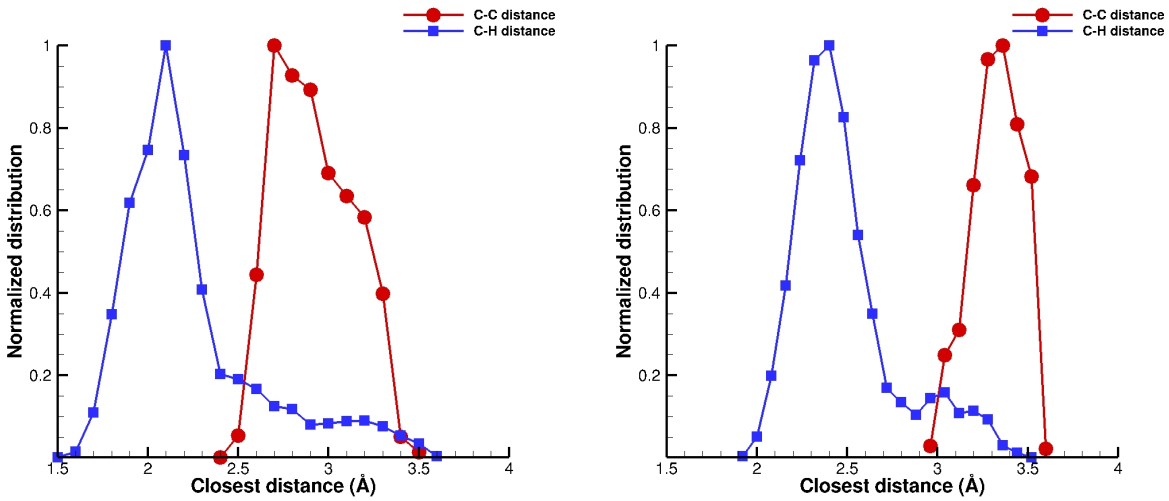

(a) Cyclohexane - CNT(6,5)

(b) n-hexane - CNT(6,5)

Figure 2.8: Distance of closest approach between the organics molecules (cyclohexane, n-hexane) and CNT(6,5)

REFERENCES

[1] B. Wang, B. V. Cunning, S.-Y. Park, M. Huang, J.-Y. Kim, and R. S. Ruoff, "Graphene coatings as barrier layers to prevent the water-induced corrosion of silicate glass," *ACS Nano*, vol. 10, no. 11, pp. 9794–9800, 2016.

[2] L. Liu, S. Ryu, M. R. Tomasik, E. Stolyarova, N. Jung, M. S. Hybertsen, M. L. Steigerwald, L. E. Brus, and G. W. Flynn, "Graphene oxidation: Thickness-dependent etching and strong chemical doping," *Nano Letters*, vol. 8, no. 7, pp. 1965–1970, 2008.

[3] S. Plimpton, "Fast parallel algorithms for short-range molecular dynamics," *J. Comput. Phys.*, vol. 117, no. 1, pp. 1–19, , March 1995.

[4] Z. Li, A. Borner, and D. A. Levin, "Multi-scale study of condensation in water jets using ellipsoidal-statistical bhatnagar-gross-krook and molecular dynamics modeling," *The Journal of Chemical Physics*, vol. 140, no. 22, p. 224501, 2014. [Online]. Available: https://doi.org/10.1063/1.4879797

[5] J. C. White and E. R. Davidson, "An analysis of the hydrogen bond in ice," *The Journal of Chemical Physics*, vol. 93, no. 11, pp. 8029–8035, 1990.

[6] S. Munetoh, T. Motooka, K. Moriguchi, and A. Shintani, "Interatomic potential for sio systems using tersoff parameterization," *Computational Materials Science*, vol. 39, no. 2, pp. 334 – 339, 2007.

[7] H. J. C. Berendsen, J. P. M. Postma, W. F. van Gunsteren, A. DiNola, and J. R. Haak, "Molecular dynamics with coupling to an external bath," *The Journal of Chemical Physics*, vol. 81, pp. 3684–3690, 1984.

[8] S. J. Stuart, A. B. Tutein, and J. A. Harrison, "A reactive potential for hydrocarbons with intermolecular interactions," *J. Chem. Phys.*, vol. 112, no. 14, pp. 6472–6486, April 2000.

[9] D. Neeb, D. Saile, and A. Gülhan, "Experiments on a smooth wall hypersonic boundary layer at mach 6," *Experiments in Fluids*, vol. 59, no. 4, March 2018.

[10] J. Jones, "On the determination of molecular fields. —ii. from the equation of state of a gas," *Proceedings of the Royal Society of London A: Mathematical, Physical and Engineering Sciences*, vol. 106, no. 738, pp. 463–477, 1924.

[11] M. T. Walsh, E. E. Roller, K.-S. Ko, and X. Huang, "Measurement of dna polymerase incorporation kinetics of dye-labeled nucleotides using total internal reflection fluorescence microscopy," *Biochemistry*, vol. 54, no. 26, pp. 4019–4021, 2015, pMID: 26096371.

[12] M. S. Dresselhaus, G. Dresselhaus, P. C. Eklund, and A. M. Rao, *Carbon Nanotubes*. Dordrecht: Springer Netherlands, 2000, pp. 331–379.

[13] R. Baughman, A. Zakhidov, and W. A de Heer, "Carbon nanotubes-the route toward applications," *Science (New York, N.Y.)*, vol. 297, pp. 787–92, 09 2002.

[14] G. Kresse and J. Hafner, "Ab initio molecular dynamics for liquid metals," *Phys. Rev. B*, vol. 47, pp. 558–561, Jan 1993.

[15] G. Kresse and J. Hafner, "Ab initio molecular-dynamics simulation of the liquid-metal–amorphous-semiconductor transition in germanium," *Phys. Rev. B*, vol. 49, pp. 14 251–14 269, May 1994.

[16] G. Kresse and J. Furthmller, "Efficiency of ab-initio total energy calculations for metals and semiconductors using a plane-wave basis set," *Computational Materials Science*, vol. 6, no. 1, pp. 15 – 50, 1996.

[17] G. Kresse and J. Furthmüller, "Efficient iterative schemes for ab initio total-energy calculations using a plane-wave basis set," *Phys. Rev. B*, vol. 54, pp. 11 169–11 186, Oct 1996.

[18] W. L. Jorgensen, D. S. Maxwell, and J. Tirado-Rives, "Development and testing of the opls all-atom force field on conformational energetics and properties of organic liquids," *Journal of the American Chemical Society*, vol. 118, no. 45, pp. 11 225–11 236, 1996.

[19] J. P. Perdew and A. Zunger, "Self-interaction correction to density-functional approximations for many-electron systems," *Phys. Rev. B*, vol. 23, pp. 5048–5079, May 1981.

[20] M. J. Longhurst and N. Quirke, "The environmental effect on the radial breathing mode of carbon nanotubes. ii. shell model approximation for internally and externally adsorbed fluids," *The Journal of Chemical Physics*, vol. 125, no. 18, p. 184705, 2006.

[21] M. J. Longhurst and N. Quirke, "The environmental effect on the radial breathing mode of carbon nanotubes in water," *The Journal of Chemical Physics*, vol. 124, no. 23, p. 234708, 2006.

[22] Y. Wu and N. R. Aluru, "Graphitic carbon- water nonbonded interaction parameters," *The Journal of Physical Chemistry B*, vol. 117, no. 29, pp. 8802–8813, 2013, pMID: 23802763.